Monthly Notices
of the
ROYAL ASTRONOMICAL SOCIETY

MNRAS **458,** 2694–2709 (2016)
Advance Access publication 2016 March 1

doi:10.1093/mnras/stw468

Problems for the WELS classification of planetary nebula central stars: self-consistent nebular modelling of four candidates

Hassan M. Basurah,[1] Alaa Ali,[1,2★] Michael A. Dopita,[1,3] R. Alsulami,[1] Morsi A. Amer[1,2] and A. Alruhaili[1]

[1]*Astronomy Department, Faculty of Science, King Abdulaziz University, 21589 Jeddah, Saudi Arabia*
[2]*Department of Astronomy, Faculty of Science, Cairo University, 12613, Egypt*
[3]*Research School of Astronomy and Astrophysics, Australian National University, Cotter Rd., Weston, ACT 2611, Australia*

Accepted 2016 February 25. Received 2016 February 25; in original form 2015 October 15

ABSTRACT

We present integral field unit (IFU) spectroscopy and self-consistent photoionization modelling for a sample of four southern Galactic planetary nebulae (PNe) with supposed weak emission-line central stars. The Wide Field Spectrograph on the ANU 2.3 m telescope has been used to provide IFU spectroscopy for NGC 3211, NGC 5979, My 60, and M 4-2 covering the spectral range of 3400–7000 Å. All objects are high-excitation non-Type I PNe, with strong He II emission, strong [Ne V] emission, and weak low-excitation lines. They all appear to be predominantly optically thin nebulae excited by central stars with $T_{\rm eff} > 10^5$ K. Three PNe of the sample have central stars which have been previously classified as weak emission-line stars (WELS), and the fourth also shows the characteristic recombination lines of a WELS. However, the spatially resolved spectroscopy shows that rather than arising in the central star, the C IV and N III recombination line emission is distributed in the nebula, and in some cases concentrated in discrete nebular knots. This may suggest that the WELS classification is spurious, and that, rather, these lines arise from (possibly chemically enriched) pockets of nebular gas. Indeed, from careful background subtraction we were able to identify three of the sample as being hydrogen rich O(H)-Type. We have constructed fully self-consistent photoionization models for each object. This allows us to independently determine the chemical abundances in the nebulae, to provide new model-dependent distance estimates, and to place the central stars on the Hertzsprung–Russell diagram. All four PNe have similar initial mass ($1.5 < M/{\rm M}_\odot < 2.0$) and are at a similar evolutionary stage.

Key words: plasmas – ISM: abundances – planetary nebulae: individual: NGC 3211 – planetary nebulae: individual: NGC 5979 – planetary nebulae: individual: My 60 – planetary nebulae: individual: M 4-2.

1 INTRODUCTION

Planetary nebulae (PNe) represent an advanced stage in the evolution of low- and intermediate-mass stars as they make the transition between the asymptotic giant branch (AGB) and the white dwarf (WD) stages. The gaseous nebula which appears now as a PN is the remnant of the deep convective envelope that surrounded the central core of AGB. This core is now revealed as the central star (CS) of the PN. Thus, the PNe provide fundamental data on the mass-loss processes during the AGB stage, the chemical enrichment of the envelope by dredge-up processes, as well as information about the mass, and effective temperature of the remaining stellar core.

★E-mail: afmali@kau.edu.sa

Up to now, most studies of the emission-line spectra of PNe have been derived from long-slit spectroscopic work. However, an accurate derivation of the physical conditions and chemical abundances in the nebular shell relies upon knowledge of the integrated spectra. For Galactic PNe, this can only be determined using integral field spectroscopic instruments. This field was pioneered by Monreal-Ibero et al. (2005) and Tsamis et al. (2007), although it is only recently that detailed physical studies using optical integral field data have been undertaken, amongst which we can cite Monteiro et al. (2013, NGC 3242), Danehkar, Parker & Ercolano (2013, SuWt 2), Danehkar et al. (2014, Abell 48), Danehkar & Parker (2015, Hen 3-1333 and Hen 2-113), and Ali et al. (2015b, PN G342.0−01.7). In this paper, we will analyse integral field data obtained with the Wide Field Spectrograph (WiFeS) integral field spectrograph (Dopita et al. 2007, 2010) to derive plasma

diagnostics, chemical composition, and kinematical parameters of the four highly excited nebulae NGC 3211, NGC 5979, My 60, and M 4-2 and to study the properties of the CSs of these objects, which from the evidence of their spectra alone appear to belong to the class of weak emission-line stars (WELS; Tylenda, Acker & Stenholm 1993), whose properties are described below.

Reviewing the literature, none of our target objects have been subject to an individual detailed study. However, many of their nebular properties and CS characteristics have been derived, and the results are distributed amongst a large number of papers, particularly in the cases of NGC 3211 and NGC 5979. From imaging data, the nebula NGC 3211 was classified as an elliptical PN (Górny et al. 1999) with an extended halo of radius ~ 3.2 times that of the main nebular shell (Baessgen & Grewing 1989). The plasma diagnostics and elemental abundances of the object were studied in a few papers (Perinotto 1991; Milingo, Henry & Kwitter 2002). The CS of NGC 3211 has several temperature and luminosity estimates: 135 kK and 2500 $L_{\odot}$ (Shaw & Kaler 1989), 155 kK and 345 $L_{\odot}$ (Gathier & Pottasch 1989), and 150 kK and 1900 $L_{\odot}$ (Gruenwald & Viegas 1995). Gurzadian (1988) provided upper and lower estimates of CS temperature of 89 and 197 kK, respectively.

The morphology of NGC 5979 was studied clearly from the narrow-band [O III] image taken by Corradi et al. (2003). The object was classified as an elliptical PN surrounded by a slightly asymmetrical halo. Another [O III] image from the *Hubble Space Telescope* taken by Hajian et al. (2007) shows a similar structure, but at better resolution. Phillips (2000) suggested that such haloes likely arise through the retreat of ionization fronts within the nebular shell, as the CS temperature and luminosity decline at intermediate phases of PN evolution. The CS of NGC 5979 was classified as a WELS by Weidmann & Gamen (2011), but later Górny (2014) claimed that the key CS emission-line features of the WELS type, and C IV at 5801–12 Å and N III, C III, and C IV complex feature at 4650 Å can be of nebular origin. Stanghellini, Corradi & Schwarz (1993) reported remarkably small values of both the temperature (58 kK) and luminosity (71 $L_{\odot}$) of NGC 5979 CS. However, these estimates were based on the H I Zanstra temperature method, which can be considerably in error if the nebula is optically thin. More likely values for the CS temperature (100 kK) and luminosity (14 000 $L_{\odot}$) were given by Corradi et al. (2003). The details of the chemical composition of NGC 5979 have been studied in the optical regime by Kingsburgh & Barlow (1994) and Górny (2014).

Ruffle et al. (2004) presented an Hα contour map of My 60 that shows a circular or only mildly elliptical morphology of the object. From the velocity measurements of the nebular shells, Corradi et al. (2007) found that one side of the nebular shell has lower expansion velocity than the opposite side. Stanghellini et al. (1993) reported that My 60 is an elliptical PN with multiple shell and its CS has an effective temperature of 113 kK and luminosity of 4216 $L_{\odot}$. A detailed spectroscopic study of My 60 and its CS was recently made by Górny (2014), where they derived the nebular chemical composition and classified its CS as a WELS type.

Weidmann & Gamen (2011) presented a low-resolution spectrum for the CS of the M 4-2 nebula which revealed the characteristic emission lines of WELS type. For this object, Zhang & Kwok (1993) reported a stellar temperature of 101 kK and a luminosity of 5600 $L_{\odot}$. The Hα and [O III] images presented by Schwarz, Corradi & Melnick (1992) reveal a roughly circular nebula with unresolved internal structure. Weak constraints on the nebular temperature, density, and chemical composition were given by Kaler et al. (1996).

Our interest in studying this particular group of PNe is that all four appear to be members of the (carbon-rich) WELS class of CSs. The WELS denomination proposed by spectral characteristics of this class was described in detail by Marcolino & de Araújo (2003), who argue that there seems to be a general evolutionary sequence connecting the H-deficient CSs and the PG 1159 stars which link the PN stars to WDs. The proposed evolutionary sequence originally developed by Parthasarathy, Acker & Stenholm (1998) is [WCL] → [WCE] → WELS → PG 1159.

Fogel, De Marco & Jacoby (2003) were unsuccessful in finding an evolutionary sequence for WELS similar to what had been established for the [WR] CS. However, they found that WELS have intermediate stellar temperature (30–80 kK). They found no WELS associated with Type I PNe – all studied objects having N/O ratios lower than 0.8, indicating lower mass precursors. However, we should note here that the lower limit of the N/O ratio in Type I PNe is 0.5 as defined by Peimbert & Torres-Peimbert (1983, 1987). Adopting this criterion of Type I PNe to the analysis of Fogel et al. (2003) would imply that ∼20 per cent (5 objects) of the sample (26 objects) are of Type I (fig. 2, Fogel et al. 2003). Girard, Köppen & Acker (2007) affirm, on average, WELS have slightly lower helium and nitrogen abundances compared to [WR] and non-WR PNe. They find somewhat enhanced helium and nitrogen abundances in [WR] PNe with an N/O ratio ∼4 times solar value, while WELS have N/O ratios which are nearly solar value. From the *IRAS* two-colour diagram, they find that WELS are shifted to bluer colours than the other [WR] PNe. Frew & Parker (2012) show that WELS have larger scaleheight compared to other many CS classes and consequently they rise from low-mass progenitor stars.

The emission lines which characterize the WELS spectral class are the recombination lines of C and N and consist of the following: N III λλ4634, 4641, C III λ4650, C IV λ4658, and C IV λλ5801, 5812. These lines are indistinguishable in width from the nebular lines, although on low-dispersion spectra the group of lines around 4650 Å and the C IV doublet around 5805 Å may appear to be broad features. Frew & Parker (2012) noted that the characteristic WELS recombination lines such as C III, C IV, and N III were also observed in some massive O-type stars, as well as in low-mass X-ray binaries and cataclysmic variables. Corradi et al. (2011) observed these C III, C IV, and N III emission lines in the spectrum of the close binary CS of the highly excited PN IPHASX J194359.5+170901. Also, Miszalski et al. (2011) explained that many of the characteristic WELS emission lines have been observed in close binary CSs of PNe such as the high-latitude PN ETHOS 1. Further, they note that lines originate from the irradiated zone on the side of the companion facing the primary. On this basis, Miszalski (2009) claims that many of WELS are likely to be misclassified as close binaries.

It has been difficult to characterize the exact evolutionary state or nature of the WELS class. For example, from UV data, Marcolino et al. (2007) find lower terminal velocities than those characterizing the [WC] – PG 1159 stars, arguing that the latter form a distinct class. Weidmann, Méndez & Gamen (2015) used medium-resolution spectra taken with the Gemini Multi-Object Spectrograph to discover that 26 per cent of them are H-rich O stars, and at least 3 per cent are H-deficient. They argue against the denomination of WELS as a spectral type, since the low-resolution spectra generally used to provide this classification do not provide enough information about the photospheric H abundance. In addition, we have the disturbing conclusion by Górny (2014) that in NGC 5979 the strong recombination line emission arises not in the CS, but in the surrounding nebula.

The literature on the WELS class will be more extensively discussed below, but it is clear from the above discussion that high spectral resolution integral field data should cast light on the

Table 1. A summary of the observing log.

Nebula name	PNG number	No. of frames	Exposure time (s)	Date	Airmass	v_{hel} corr. (km s^{-1})	Standard stars used
NGC 3211	PN G286.3−04.8	6	100	31/3/2014	1.19	2.98	HD 111980 and HD 031128
		3	600	31/3/2014	1.2	2.98	HD 111980 and HD 031128
NGC 5979	PN G322.5−05.2	6	300	30/3/2014	1.25	20.0	HD 111980 and HD 160617 and HD 031128
		3	600	30/3/2014	1.18	20.0	HD 111980 and HD 160617 and HD 031128
My 60	PN G283.8+02.2	3	200	30/3/2014	1.12	1.5	HD 111980 and HD 160617 and HD 031128
		3	600	30/3/2014	1.1	1.5	HD 111980 and HD 160617 and HD 031128
M 4-2	PN G248.8−08.5	6	300	30/3/2014	1.0	−14.8	HD 111980 and HD 160617 and HD 031128

evolutionary status of the WELS. Such data are presented in this paper. The observations and the data reduction are described in Section 2, while the physical conditions, ionic and elemental abundance determinations are given in Section 3. Section 4 is dedicated to study the expansion and radial velocities of the sample. In Section 5, we discuss the pieces of evidence that prove that the PN CSs cannot be classified as WELS type. A full discussion on the global photoionization models is provided in Section 6.

2 THE INTEGRAL FIELD OBSERVATIONS

2.1 Observations

The integral field spectra of the PNe were obtained over two nights of 2013 March 30 and 31 with the WiFeS (Dopita et al. 2007, 2010) mounted on the 2.3 m ANU telescope at Siding Spring Observatory (Mathewson et al. 2013). The WiFeS instrument delivers a field of view of 25 arcsec × 38 arcsec at a spatial resolution of either 1.0 arcsec × 0.5 arcsec or 1.0 arcsec × 1.0 arcsec, depending on the binning on the CCD. In these observations, we used the 1.0 arcsec × 1.0 arcsec option. The blue spectral range of 3400–5700 Å was covered at a spectral resolution of ∼3000 using the B3000 grating, which corresponds to a full width at half-maximum (FWHM) of ∼100 km s^{-1}. In the red, the R7000 grating was used, which covers the spectral range of 5700–7000 Å at a higher spectral resolution $R \sim 7000$ corresponding to an FWHM of ∼45 km s^{-1}. The wavelength scale was calibrated using the Cu-Ar arc lamp with 40 s exposure at the beginning and throughout the night, while flux calibration was performed using the STIS spectrophotometric standard stars HD 111980 and HD 031128.[1] In addition, a B-type telluric standard HIP 38858 was observed to correct for the OH and H_2O telluric absorption features in the red. The separation of these features by molecular species allowed for a more accurate telluric correction which accounted for night-to-night variations in the column density of these two species.

2.2 Data reduction

All the data cubes were reduced using the PYWIFES[2] data reduction pipeline (Childress et al. 2014). A summary of the on-target spectroscopic observation log is shown in Table 1. In the long exposures, some strong nebular emission lines such as [O III] λ5007 and Hα are saturated on the CCD chip. For these, the fluxes were measured from the additional short exposure time observations.

The resultant data cubes are summed from the original exposures, cleaned of cosmic ray events, wavelength calibrated to better than 0.4 Å in the blue, and 0.07 Å in the red, corrected for instrumental sensitivity in both the spectral and spatial directions, sky background subtracted, and telluric absorption features have been fully removed. On the basis of the intrinsic scatter in derived sensitivity amongst the various standard star observations, we can estimate the error in absolute flux of these observations to be ±0.015 dex throughout the wavelength range covered by these observations.

2.3 Images

We extracted continuum-subtracted emission-line images from the data cubes using QFITSVIEW v3.1 rev.741.[3] These are then used to construct three-colour images in any desired combination of emission lines.

To illustrate the overall morphology and excitation structure of these PNe, we present in Fig. 1 images in He II (blue channel), Hβ (green channel), and [N II] (red channel). These three ions probe the excitation structure and the overall distribution of gas in these nebulae. It is clear from the incomplete shell morphology in the [N II] λ6563 line that all of these PNe are optically thin to the escape of EUV photons. In the cases of NGC 3211 and NGC 5979, the outer shell is clumpy and broken, while in the other two cases the low-excitation gas is distributed symmetrically on either side of the nebula. These cases are reminiscent of the fast, low-ionization emission regions in NGC 3242, NGC 7662, and IC 2149 and other PNe described in a series of papers (Balick et al. 1993, 1994, 1998; Hajian et al. 1997), and discussed on a theoretical basis by Dopita (1997). In the case of My 60, the existence of Fast Low Ionization Emission Regions (FLIERs) may well be the cause of the asymmetric expansion reported by Corradi et al. (2007). The double-shell structure of NGC 5979 is clearly evident.

2.4 Global spectra

In order to build a detailed photoionization model of the PN, a mean spectrum of the whole nebula is required. From the 3D data cube, we extracted this spectrum using a circular aperture which matched the observed extent of the bright region of the PNe using QFITSVIEW. The residuals of the night sky lines of [O I] λ5577.3, [O I] λ6300.3, and [O I] λ6363.8 were removed by hand. The scaling between the blue and red spectra caused by slight mismatch of the extraction apertures was improved by measuring the total fluxes in

[1] Available at www.mso.anu.edu.au/∼bessell/FTP/Bohlin2013/GO12813.html
[2] http://www.mso.anu.edu.au/pywifes/doku.php
[3] QFITSVIEW v3.1 is a FITS file viewer using the QT widget library and was developed at the Max Planck Institute for Extraterrestrial Physics by Thomas Ott.

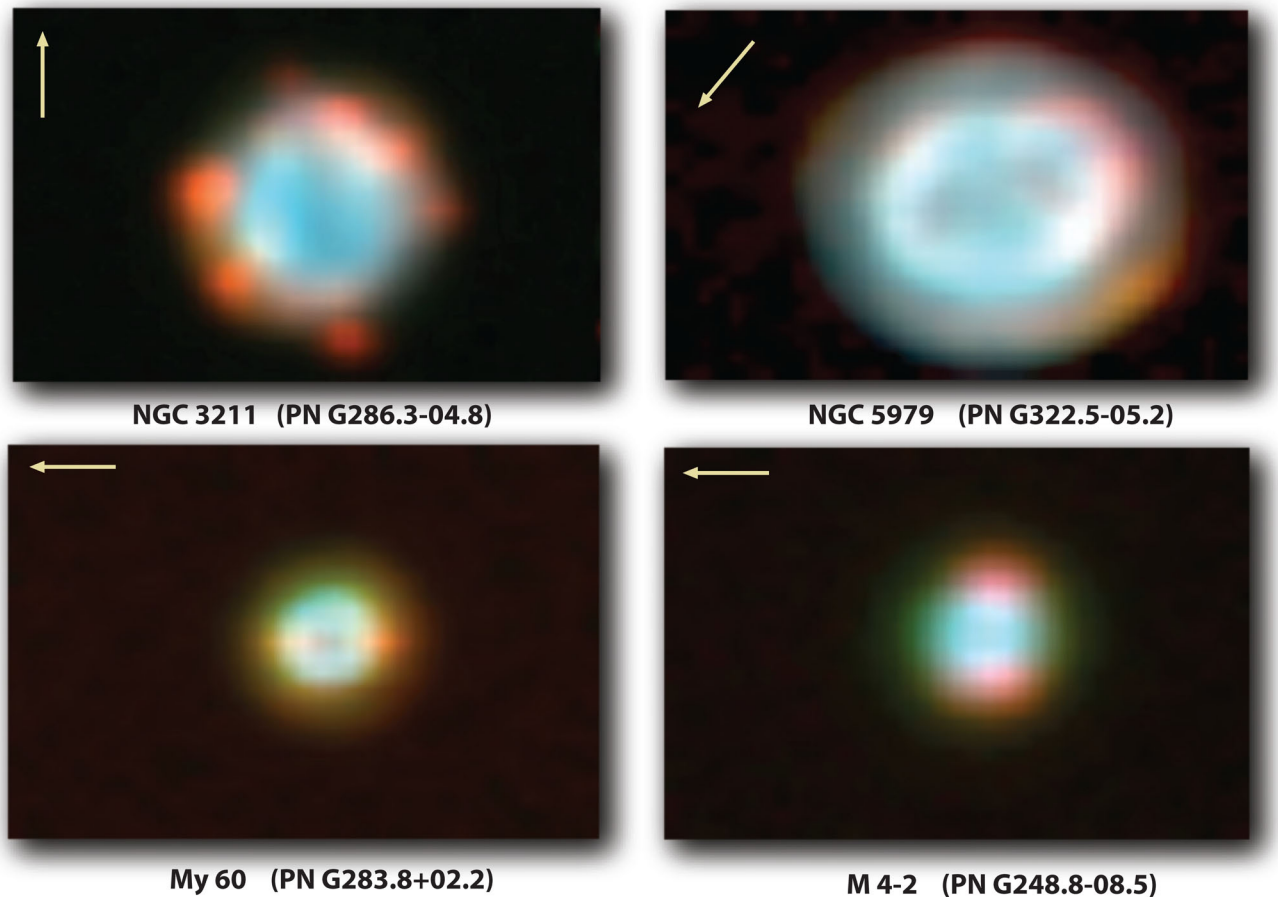

Figure 1. Narrow-band continuum-subtracted image composites of our PNe derived from the WiFeS data cubes. The field size of each image is 25 arcsec × 38 arcsec. The yellow arrow denotes the direction of north in each image. The colour coding of these images is He II λ4686 (blue), Hβ (green), and [N II] λ6583 (red), and they are presented on a square root stretch to bring out the fainter features. Each image has been boxcar smoothed by 1 spaxel or 1.0 arcsec to remove sharp spaxel boundaries. Note that all objects have only fragmentary shells of [N II] emission, which indicates that all four objects are optically thin to the escape of ionizing radiation.

the common spectral range between blue and red channels (5500–5700 Å), and applying the scale factor to the red spectrum to match the two measured fluxes.

We measured emission-line fluxes from the final combined, flux-calibrated blue and red spectra of each PN. The line fluxes and their uncertainties were measured using the IRAF `splot`[4] task and were integrated between two given limits, over a local continuum fitted by eye, using multiple Gaussian fitting for the line profile. We used the Nebular Empirical Abundance Tool (NEAT;[5] Wesson, Stock & Scicluna 2012) to derive the reddening coefficients and in the subsequent plasma diagnostics and ionic and elemental abundance calculations. The derived logarithmic reddening coefficients and the Hβ fluxes are given in Table 2, and the complete list of line intensities is given in Table A1 of Appendix A.

[4] IRAF is distributed by the National Optical Astronomy Observatory, which is operated by the Association of Universities for Research in Astronomy (AURA) under a cooperative agreement with the National Science Foundation.

[5] The code, documentation, and atomic data are freely available at http://www.sc.eso.org/rwesson/codes/neat/

3 DETERMINATION OF PHYSICAL CONDITIONS

3.1 Temperatures and densities

The spectral lines in the sample given in Table A1 allow us to determine the electron densities from the low- and medium-ionization zones and the electron temperature from the low-, medium-, and high-ionization zones. The lines of low ionization were used to determine the nebular densities from the [S II] λ6716/λ6731 and [O II] λ3727/λ3729 and the temperatures from [N II] (λ6548 + λ6584)/λ5754 line ratios, while in the more highly ionized zones we determine the nebular densities from the [Cl III] λ5517/λ5537, [Ar IV] λ4711/λ4740, and [Ne IV] λ4715/λ4726 line ratios, and the temperature is estimated from the [O III] (λ4959 + λ5007)/λ4363 line ratio. For NGC 5979, we are also able to determine the nebular temperature from the high-ionization line ratio [Ar V] (λ6435 + λ7005)/λ4625. The Monte Carlo technique was used by NEAT to propagate the statistical uncertainties from the line flux measurements through to the derived abundances. In Table 3, we list the inferred nebular densities, temperatures, and their uncertainties for each object. In addition, we provide comparisons of our results with those which have previously appeared in the literature. In general, we find good agreement with other results.

Table 2. Reddening coefficients, observed Hβ fluxes, excitation classes, and inferred distances of our sample.

Object	c(Hβ)		Log F(Hβ)		EC		Distance (kpc)	
	This paper	Literature	This paper	Literature	(6)	(7)	(8)	(9)
NGC 3211	0.37	0.34(1), 0.32(2), 0.25(3)	−11.12	−11.06(2), −11.39(3)	10.1	9.1	2.61	2.59
NGC 5979	0.40	0.38(1), 0.25(4)	−11.34	−11.23(2), −11.9(5)	10.8	10.1	2.99	2.49
My 60	0.86	0.91(1), 0.95(2), 0.87(4)	−11.83	−11.78(2), −11.8(5)	10.4	8.8	3.76	3.33
M 4-2	0.57	0.37(1)	−11.85	−11.70(5)	9.5	9.0	5.91	5.72

References: (1) Tylenda et al. (1992); (2) Shaw & Kaler (1989); (3) Milingo et al. (2002); (4) Górny (2014); (5) Acker et al. (1991); (6) Reid & Parker (2010); (7) Meatheringham & Dopita (1991); (8) Ali, Ismail & Alsolami (2015a); (9) Frew, Parker & Bojičić (2016), assuming that all objects are optically thin.

Table 3. Electron temperatures and densities measured for the PN sample, and fitted using global photoionization modelling.

	Temperature (K)				Density (cm^{-3})				
Object	[O III]	[N II]	[S II]	[Ar V]	[S II]	[O II]	[Ar IV]	[Cl III]	[Ne IV]
NGC 3211									
Measured:	13 937 ± 162	11 892 ± 587			1363 ± 270	1601 ± 134	1583.6 ± 317	1048 ± 848	
Nebular model:	14 810	11 910	10 910	17 040	1370	1684	1464	1538	1310
Ref (1)	13 300	10 300			1200				
Ref (2)	14 320								
Ref (3)	14 000	12 500				970			
NGC 5979									
Measured:	13 885 ± 234	13 578 ± 1217		14 375 ± 902	1470 ± 320	2034 ± 261	1342 ± 503	1342 ± 503	
Nebular model:	13 860	13 640	13 690	15 180	1680	1695	1625	1667	1583
Ref (4)					1549	1585	1862	2570	
Ref (5)		$14\,604^{+15\,206}_{-14\,049}$			509^{+849}_{-240}				
Ref (6)	13 100					1410			
My 60									
Measured:	13 665 ± 229	13 411 ± 688			2098 ± 215	3009 ± 706	1763 ± 472	1637 ± 945	
Nebular model:	13 210	13 270	13 340	15 250	2132	2150	2045	2113	
Ref (5)		$13\,868^{+14\,412}_{-13\,324}$			1510^{+2450}_{-1050}				
M 4-2									
Measured:	15 170 ± 186	11 084 ± 380			1662 ± 78	2178 ± 235	1537 ± 486	1164 ± 864	
Nebular model:	14 070	12 080	11 350	16 870	1775	2088	1680	2027	1745

References: (1) Henry, Kwitter & Balick (2004); (2) Kaler et al. (1996); (3) Liu & Danziger (1993); (4) Wang et al. (2004); (5) Górny (2014); (6) Kingsburgh & Barlow (1994).

Table 3 also gives the values of the density and temperature derived from the global photoionization models which are presented in detail and discussed in Section 6, below.

3.2 Excitation classes and distances

The detected emission lines in all objects cover a wide range of ionization states from neutral species such as [O I] all the way up to [Ne V] which requires the presence of photons with greater energy than 97.1 eV. For medium- and high-excitation classes (EC), above EC = 5, the line ratio of He II λ4686 Å/Hβ provides the best indication of EC of the nebula. This line is only present when the CS has an effective temperature, $T_{\rm eff}$ > 85 000 K. Based on the analysis of 586 PNe in the Large Magellanic Cloud, Reid & Parker (2010) compared the three main classification schemes of Aller (1956), Meatheringham & Dopita (1991), and Stanghellini et al. (2002) to estimate the EC of PNe. They noticed that at EC ≥5, the line ratio [O III]/Hβ is not fixed but it increases to some degree with nebular excitation. Therefore, they introduced a new method to incorporate both the He II λ4686 Å/Hβ and [O III]/Hβ line ratios in classifying the EC of the nebula. Here we present (Table 2) the EC for the four objects using both methods of Reid & Parker (2010) and Meatheringham & Dopita (1991).

Determining a reliable distance for a PN is not an easy task. To determine the distance of PN, one should rely first on the individual methods, then on the statistical methods. A summary on the applications, assumptions, limitations, and uncertainties of individual methods was given in Ali et al. (2015a) and Frew et al. (2016). Considering the individual distances in the literature, we found that NGC 3211 and NGC 5979 have each two distance estimates, and My 60 has only one. NGC 3211 has distances of 1.91 kpc (Gathier, Pottasch & Pel 1986 – extinction method) and 3.7 kpc (Zhang 1993 – gravity method). The latter technique should be the most reliable in this case. NGC 5979 has distances of 2.0 kpc (Frew et al. 2016 – expansion method) and 5.8 kpc (Zhang 1993 – gravity method). My 60 has a distance of 3.2 kpc (Zhang 1993 – gravity method). On average, Ali et al. (2015a) find that the gravity method overestimates the PN distance by ∼25 per cent compared to other methods. It is also obvious here that a large variation exists between the various distance estimates of NGC 3211 and NGC 5979. This discrepancy in distance estimates commonly appears, not only among different methods, but sometimes between different authors using the same method (Ali et al. 2015a). Lacking trusted individual distances, e.g. trigonometric or cluster membership distances, for any of the sample, we rely initially on the statistical methods. For each PN in our sample, we derived two statistical distances which are given in Table 2. The first value was deduced from the distance scale

Table 4. Abundances derived from the NEAT and MAPPINGS codes for NGC 3211 and NGC 5979. Model I refers to the total abundances in the photoionization model, while model II refers to gas phase abundances in the same model.

	NGC 3211						NGC 5979			
Element	NEAT	Model I	Model II	Ref 1	Ref 2	Ref 3	NEAT	Model I	Model II	Ref 4
He/H	1.06E−1 ± 2.7E−3	1.10E−1	1.10E−1	1.10E−1		1.17E−1	1.10E−1 ± 3.9E−3	1.10E−1	1.10E−1	$1.11E-1^{+1.17E-1}_{-1.05E-1}$
C/H	1.20E−3 ± 6.7E−5	1.34E−3	8.64E−4				2.05E−3 ± 1.3E−4	1.84E−3	1.19E−3	
N/H	1.15E−4 ± 9.9E−6	7.96E−5	6.62E−5	1.63E−4			1.38E−4 ± 1.2E−5	2.81E−5	2.33E−5	$6.70E-5^{+7.62E-5}_{-5.62E-5}$
O/H	4.43E−4 ± 2.0E−5	4.60E−4	2.97E−4	8.38E−4	5.00E−4	8.77E−4	4.55E−4 ± 3.0E−5	6.21E−4	3.74E−4	$3.44E-4^{+4.06E-4}_{-2.87E-4}$
Ne/H	9.30E−5 ± 3.9E−6	7.82E−5	7.82E−5	1.31E−4	1.38E−4		5.63E−5 ± 7.8E−6	6.05E−5	6.05E−5	$5.75E-5^{+6.59E-5}_{-5.13E-5}$
Ar/H	1.90E−6 ± 9.6E−8	1.60E−6	1.60E−6	6.33E−6			2.17E−6 ± 1.3E−7	2.17E−6	2.17E−6	$2.27E-6^{+2.48E-6}_{-2.03E-6}$
K/H		8.07E−7	8.07E−7							
S/H	6.18E−6 ± 4.83E−7	5.41E−6	5.41E−6	4.40E−6	1.34E−5		8.48E−6 ± 7.3E−7	3.92E−6	3.92E−6	$5.32E-6^{+5.92E-6}_{-4.62E-6}$
Cl/H	1.46E−7 ± 1.44E−8	5.40E−7	1.45E−7	4.52E−7			1.90E−7 ± 1.6E−8	4.20E−7	1.13E−7	$9.30E-6^{+1.13E-5}_{-6.87E-6}$
Fe/H			6.80E−8						2.97E−8	
N/O	0.26	0.17	0.23				0.23	0.06	0.08	

Note. The abundances of K and C elements in models I and II were calculated from [K IV] and C II λ4267 emission lines, respectively. References: (1) Henry et al. (2004); (2) Maciel & Quireza (1999); (3) Liu & Danziger (1993); (4) Górny (2014).

of Ali et al. (2015a), while the second value was taken from that of Frew et al. (2016). We find small distance variations between both distance scales (∼1–17 per cent), assuming that all objects are optically thin PNe (Table 2). In this paper, we have adopted the nebular distances derived from the distance scale of Ali et al. (2015a). These distances may be compared with those derived in Section 6.2 (below).

On the basis of these distances, we derived absolute luminosities $L_{H\beta}$: 1.44×10^{34}, 1.24×10^{34}, 1.79×10^{34}, and 2.20×10^{34} erg s^{-1} for NGC 3211, NGC 5979, My 60, and M 4-2, respectively.

3.3 Ionic and elemental abundances

Applying the NEAT, ionic abundances of nitrogen, oxygen, neon, argon, chlorine, and sulphur were calculated from collisional excitation lines, while helium and carbon were calculated from optical recombination lines using the temperature and density appropriate to their ionization potential. When several lines from a given ion are present, the ionic abundance adopted is found by averaging the abundances from each ion and weighted according to the observed intensity of the line. The total abundances were calculated from ionic abundances using the ionization correction factors (ICF) given by Kingsburgh & Barlow (1994), to correct for unseen ions.

The total helium abundances for all objects were determined from He^+/H and He^{2+}/H ions. The total carbon abundances were determined from C^{2+}/H and C^{3+}/H ions for all objects, except My 60 which is determined from C^{2+}/H ion only, using ICF (C) = 1.0.

None of the objects studied here has He/H ≥ 0.125 and/or N/O ≥0.5. Therefore, they cannot be classified as a Type I according to the original classification scheme proposed by Peimbert (1978). This probably implies that their progenitor stars had lower initial masses ($M < 4\,M_\odot$). According to the derived chemical compositions of the objects, they are most likely to be classified as Types II and III. These types of PNe have abundances which more nearly reflect the properties of the interstellar medium out of which their CSs have been formed, particularly with respect to those chemical elements that are not contaminated by the evolution of intermediate-mass stars, such as oxygen, neon, sulphur, and argon. The He/H, N/H, and N/O abundances in NGC 3211 and NGC 5979 are consistent with Type IIa PNe (Quireza, Rocha-Pinto & Maciel 2007). The Galactic vertical height ($z \leq 1$ kpc) and peculiar velocity (≤60 km s^{-1}) of NGC 3211 confirm that it is probably a member of Galactic thin disc. The chemistry of My 60 and M 4-2 is consistent with Type IIb/III PNe, both nebulae have Galactic vertical heights less than 1 kpc, but peculiar velocities larger than 60 km s^{-1}. Therefore, we suggest that both objects are of Type III PNe, which are usually located in the Galactic thick disc. These results are consistent with that of Fogel et al. (2003) and Girard et al. (2007) where none of WELS are associated with Type I PNe.

Tables 4 and 5 compare the abundance determinations of the four objects with those obtained by our detailed global photoionization models and with those given by other authors.

4 EXPANSION AND RADIAL VELOCITIES

The expansion velocity is an essential quantity to determine in order to understand nebular evolution. We used three emission lines ([S II], [N II], [Ar V]) that all lie in the red part of the WiFeS spectrum, and are consequently observed at higher spectral resolution ($R = 7000$) than the blue spectra ($R = 3000$). These lines were used to determine the nebular expansion velocity V_{exp} for each object. The FWHM of each line was measured using the IRAF `splot` task. The full width was corrected for instrumental and thermal broadening to derive the expansion velocity using the following formula (Gieseking, Hippelein & Weinberger 1986)

$$V_{exp} = 0.5\left[w_{obs}^2 - w_{inst}^2 - 8(\ln 2)kT_e/m\right]^{1/2}, \quad (1)$$

where w_{obs} is the observed FWHM of the measured line, w_{inst} is the instrumental FWHM, k is Boltzmann's constant, T_e is the nebular temperature, and m is the atomic mass of the species emitting the measured line. The results are given in Table 6. As expected from the ionization stratification of these PNe, the measured expansion velocity decreases with increasing ionization potential of the ion. Apparently, there are no previous attempts to measure the expansion velocity of M 4-2. NGC 3211 has measured velocities of 26.5, 31.0, and 21.1 km s^{-1} using the [O III], [O II] and He II emission lines, respectively (Meatheringham, Wood & Faulkner 1988). Our derived expansion velocities for NGC 3211 in the [N II] and [S II] are smaller than those of Meatheringham et al. (1988), except for He II line. This may be attributed to the derivation of the expansion velocity from an integrated spectrum over the whole object, while other authors

Table 5. Abundances derived from the NEAT and MAPPINGS codes for My 60 and M 4-2. Model I refers to the total abundances, while model II refers to gas phase abundances in the same model.

Element	My 60				M 4-2			
	NEAT	Model I	Model II	Ref 1	NEAT	Model I	Model II	Ref 2
He/H	1.10E−1 ± 3.9E−3	1.10E−1	1.10E−1	$1.10E{-}1^{+1.16E-1}_{-1.03E-1}$	9.81E−2 ± 2.7E−3	1.04E−1	1.04E−1	1.14E−1
C/H	6.31E−4 ± 1.2E−4	1.16E−3	7.50E−4		2.58E−3 ± 1.2E−4	1.71E−3	1.19E−3	
N/H	6.85E−5 ± 7.5E−6	4.98E−5	4.14E−5	$5.11E{-}5^{+6.40E-5}_{-4.17E-5}$	5.73E−5 ± 3.8E−6	5.74E−5	5.24E−5	1.97E−4
O/H	3.15E−4 ± 2.0E−5	4.60E−4	2.97E−4	$3.15E{-}4^{+3.80E-5}_{-2.62E-4}$	2.40E−4 ± 1.1E−5	2.08E−4	1.62E−4	4.70E−4
Ne/H	6.20E−5 ± 3.9E−6	6.81E−5	6.81E−5	$6.02E{-}5^{+6.92E-5}_{-5.24E-5}$	4.85E−5 ± 2.1E−6	4.26E−5	4.26E−5	
Ar/H	1.59E−6 ± 1.1E−7	2.20E−6	2.20E−6	$1.68E{-}6^{+1.86E-6}_{-1.48E-6}$	9.27E−7 ± 1.5E−8	8.30E−7	8.30E−7	
K/H			1.01E−7			1.90E−7		
S/H	4.92E−6 ± 4.7E−7	4.50E−6	4.50E−6	$4.33E{-}6^{+5.10E-6}_{-3.66E-6}$	2.35E−6 ± 1.5E−7	3.80E−6		
Cl/H	1.20E−7 ± 1.4E−8	4.01E−7	1.10E−7	$8.33E{-}6^{+1.04E-5}_{-6.34E-6}$	4.48E−8 ± 4.1E−9	9.31E−8		
Fe/H			9.62E−8				6.75E−8	
N/O	0.22	0.11	0.14		0.24	0.22	0.26	

Note. The abundances of K and C elements in models I and II were calculated from the [K IV] and C II λ4267 emission lines, respectively. References: (1) Górny (2014); (2) Kaler et al. (1996).

Table 6. Radial and expansion velocities of the sample.

Object	RV_{hel} (km s^{-1})		V_{exp} (km s^{-1})		
	This paper	Literature	[S II]	[N II]	[Ar V]
NGC 3211	− 21.8 ± 3.5	−22.3 ± 1.6(1), −22.5 ± 2.8(2)	23.6	22.0	10.3
NGC 5979	30.4 ± 3.5	23.0 ± 3.0(1)	20.7	22.4	11.8
My 60	42.2 ± 3.0		24.2	24.1	< 10
M 4-2	119.1 ± 4.7		25.9	25.5	9.3

References: (1) Durand et al. (1998); (2) Schneider & Terzian (1983).

usually derive the expansion velocity at a certain nebular position using long-slit spectra. In the study of Meatheringham et al. (1988), they measured the maximum velocity for asymmetric objects set by the spectrograph slit along the nebular long axis. It is clear also from the NGC 3211 colour image in Fig. 1 that the [N II] emission is strongly concentrated in blobs located in the outer regions of the nebula. Hajian et al. (2007) gave an equatorial expansion velocity of 18 km s^{-1} for NGC 5979 derived from long-slit spectra in the [O III] emission line. This value is consistent with our measurements and slightly smaller than that derived from [S II] and [N II] emission lines, due to the higher ionization potential of the [O III] line. Schönberner, Jacob & Steffen (2005) provided two expansion velocities for the rim of My 60. They derived V_{exp} = 23.1 and 23.7 km s^{-1} from [O III] and [N II] emission lines, respectively. The latter one is in good agreement with our derived value.

The systemic velocities RV_{sys} of the sample were measured using the IRAF external package RVSAO. A weighted mean radial velocity was calculated for each object using Hα, [N II], and [S II] emission lines. The heliocentric correction was taken from the image header, to derive the heliocentric radial velocity RV_{hel} for each object. The results were listed in Table 6. The value of NGC 3211 is in good agreement with Durand, Acker & Zijlstra (1998) and Schneider & Terzian (1983). The radial velocity of NGC 5979 is higher than that derived by Schneider & Terzian (1983), RV_{hel} = 23 ± 3.0, which was taken originally from the low-dispersion spectra of Campbell & Moore (1918). Therefore, our larger value of RV_{hel} for NGC 5979, compared to that of Schneider & Terzian (1983), may be attributed to the different spectral resolution as well as to the fact that we derived the radial velocity from the integrated spectrum over the whole object, while other value was derived from a particular nebular position.

5 WHAT ARE THE CSs?

Of the over 3000 Galactic PNe currently known (Frew & Parker 2010), only 13 per cent of their stellar nuclei have been spectroscopically identified (Weidmann & Gamen 2011). According to the observed atmospheric spectra of the CSs of PNe, Mendez (1991) has assigned two types. In the first type hydrogen is the prevalent element (H-rich), while the second type is relatively free of hydrogen and the spectra are dominated by lines of helium and carbon elements (H-deficient).

In general, the H-deficient type can be divided into three main groups. The first group, the [WR] group, shows spectra with strong and broad emission lines mainly from He, C, and O, similar to the Wolf–Rayet stars of Population I. This group was divided into three subgroups: [WCL], [WCE], and [WO], according to the ionization stages of the element dominating the atmosphere (Crowther, De Marco & Barlow 1998; Acker & Neiner 2003). The second group, PG 1159, is composed of pre-WDs that have mainly absorption lines of He II and C IV in their spectra (Werner et al. 1997). The third group, [WC]-PG 1159, includes objects with similar optical spectra to the PG 1159 stars, but have strong P Cygni lines in the UV (e.g. N V λ1238 and C IV λ1549).

Tylenda et al. (1993) presented the analyses of extensive observations of a set of 77 emission-line CSs. About half of this set were classified as [WR] stars and the other half exhibited emission lines at the same wavelengths as [WR] stars, but having weaker intensities and narrower line widths. These they named 'weak emission-line stars' (WELS). The spectra of the WELS show the carbon doublet C IV λλ5801, 5812 and the λ4650 feature which is a blend of N III λλ4634, 4641, C III λ4650, and C IV λ4658. Furthermore, the spectra of WELS are highly ionized to the degree that the C IV λλ5801,

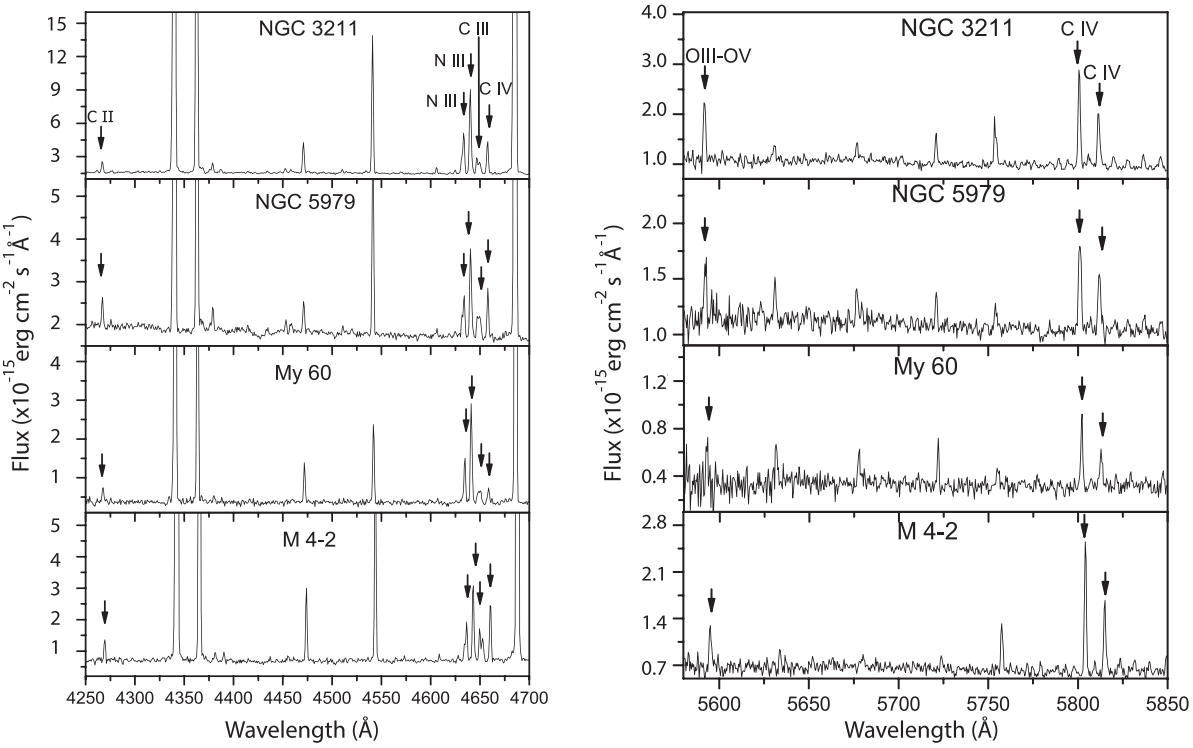

Figure 2. Characteristic emission lines generally used to classify CSs as of the WELS type, as seen in our PN sample.

5812 doublet is strong but the C III λ5696 line is either very weak or absent. Based on the analysis of the optical spectra of 31 WELS, Parthasarathy et al. (1998) found that the spectrum of a WELS is very similar to those of the [WC]-PG 1159 and PG 1159 stars. As pointed out in the introduction, they suggested that an evolutionary sequence exists connecting the [WC] CSs of PNe to the PG 1159 pre-WDs: [WC late] → [WC early] → WELS = [WC]-PG 1159 → PG 1159. Based on the UV spectra of the WELS, Marcolino et al. (2007) disagreed with Parthasarathy et al. (1998), and instead claimed that the WELS are distinct from [WC]-PG 1159 stars. They noticed that WELS type presented P Cygni features and most of their terminal velocities lie in the range from ∼1000 to 1500 km s^{-1}, while [WC]-PG 1159 stars have much higher values of ∼3000 km s^{-1}. In addition, they found that the [WC]-PG 1159 stars are characterized by several intense P Cygni emission in the ∼1150–2000 Å wavelength interval, most notably N V λ1238, O V λ1371, and C IV λ1549, while in the WELS O V λ1371 is either very weak or absent. Furthermore, Parthasarathy et al. (1998) and Marcolino & de Araújo (2003) find some absorption lines in the optical spectra of WELS such as He II λλ4541, 5412 indicating that any stellar wind is not as dense as in the case of [WR] stars.

Hajduk, Zijlstra & Gesicki (2010) claimed that not all WELS spectral type are H-deficient as [WR] stars, but some may be H-rich despite having emission lines. Recently, Weidmann et al. (2015) have observed and studied 19 WELS from the total of 72 objects known in the literature. The high-quality spectra of these objects show a variety of spectral types, where 12 of them have H-rich atmospheres, with different wind densities and only 2 objects seem to be H-deficient. They were not able to decide on the spectral type of the remaining objects, but they concluded that these objects are not [WR] stars. According to the above results, they claimed that 'the denomination WELS should not be taken as a spectral type, because, as a WELS is based on low-resolution spectra, it cannot provide enough information about the photospheric H abundance'.

Three objects of our sample have previously been associated with the WELS type: NGC 5979, M 4-2 (Weidmann & Gamen 2011), and My 60 (Górny 2014). Due to the low spectral resolution, the components of C+N λ4650 feature were not resolved in the spectra presented by Weidmann & Gamen (2011, their fig. 11) and Górny (2014, their fig. C.2). Furthermore, the components of the doublet C IV centred at 5805 Å were not resolved in the spectra given by Weidmann & Gamen (2011, their fig. 11). In Fig. 2, we illustrate our observations of the characteristic WELS emission lines seen in all four of our objects. Here, to simulate the effect of observing with a long-slit spectrograph, we extracted these spectra by taking a circle of 2 arcsec radius around the geometric centre of each object. In general, the spectra of all nebulae roughly show similar emission lines, generally identified to be of the WELS class: C II at 4267 Å, N III at 4634 and 4641 Å, C III at 4650 Å (here resolved into its two components at 4647 and 4650 Å), C IV at 4658 Å, O III–O V at 5592 Å, and finally, C IV at 5801 and 5812 Å.

Górny (2014) noticed that it was possible that – as in the case of NGC 5979 – the CS spectrum can 'mimic' the WELS type. They found that the key CS emission features of WELS type (C II at 4267 Å, N III at 4634 and 4641 Å, C III at 4650 Å, C IV at 5801 and 5812 Å) appear in a spatially extended region in the 2D spectra of NGC 5979, and therefore, they are of nebular rather than stellar origin.

To test whether the CSs in our objects were real WELS type or simply 'mimics', we constructed continuum-subtracted images in the brightest recombination lines C IV λ5801 and N III λ4641, and formed colour composites using the procedure described in Section 2.3. The result is shown in Fig. 3. From this it is evident that the recombination lines are formed in the nebula, and that the spatial separation of the C IV, N III, and [N II] emission is entirely

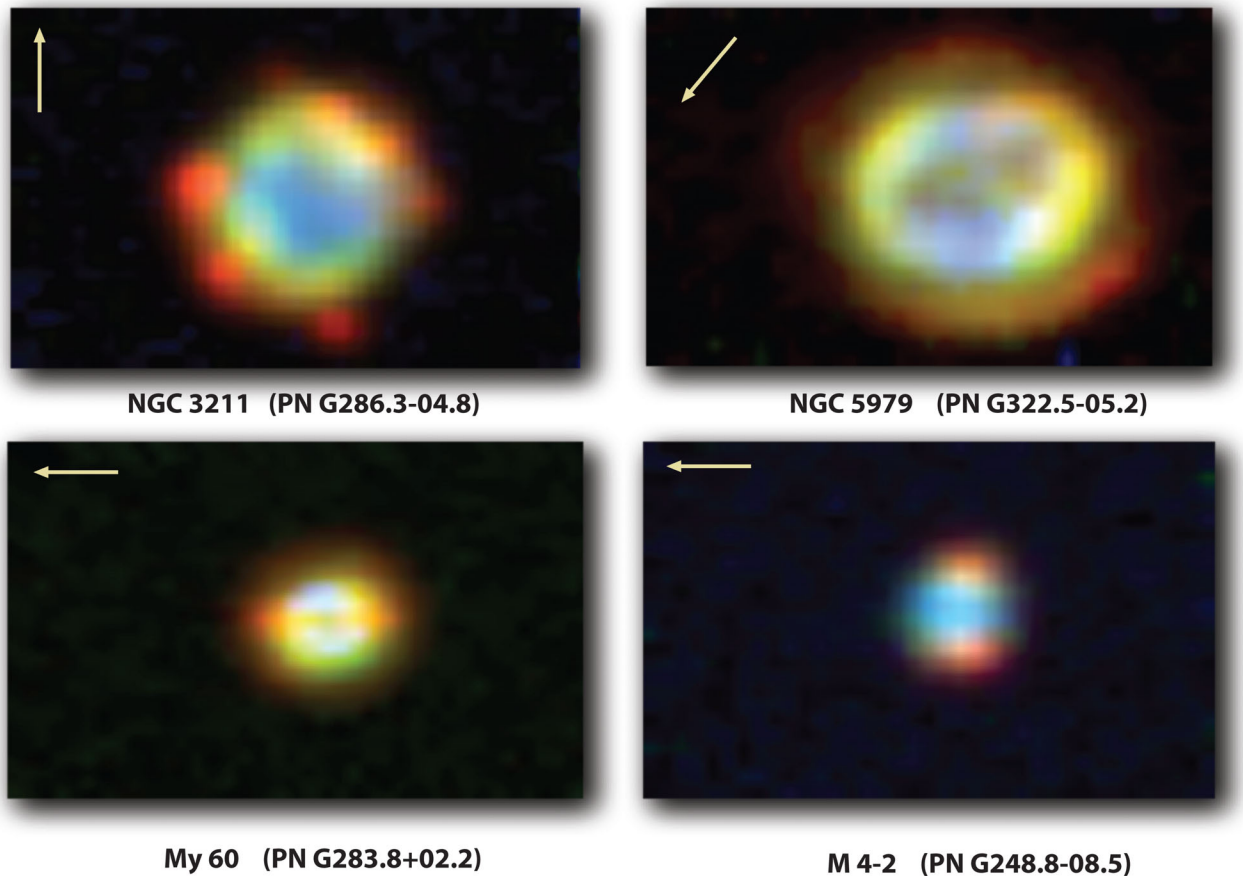

Figure 3. Narrow-band continuum-subtracted image composites of our PNe in the recombination lines of C IV λ5801 (blue), N III λ4641 (green), and [N II] λ6583 (red). As in Fig. 1, they are presented on a square root stretch to bring out the fainter features and boxcar smoothed by 1 spaxel or 1.0 arcsec to remove sharp spaxel boundaries. The arrow shows the direction of north. No trace of a CS is seen in any object. Instead, the recombination line emission of C IV and N III is – in each case – entirely of nebular origin.

consistent with ionization stratification. We therefore conclude that in every case the emission is entirely of nebular origin, and that the WELS classification is spurious for these objects.

Certainly, the CSs are detected, but if not of the WELS type, what could they be? In order to examine this, we need to carefully remove the nebular emission. This was possible in three cases: NGC 3211, NGC 5979, and My 60. The result is shown in Fig. 4 for NGC 5979. There are broad Balmer absorption features present in the blue continuum of the star, and three stellar emission lines, O VI λλ3811.3, 3834.2 and O V λ4664.4.[6] The presence of broad Balmer absorption in the CS proves the presence of H in the atmosphere, and establishes that the CS is likely to be H-burning. However, the source of the narrow O VI and O V lines remains uncertain. Being narrow, they most likely have their origin in or close to the photosphere, rather than in the wind. We tentatively classify this star, following the CS classification scheme of Mendez (1991), as O(H)-Type. These features clearly originate in the CS as can be seen from the continuum-subtracted emission-line maps shown as thumbnail images in Fig. 4. In the case of NGC 3211 and My 60, only the O VI λλ3811.3, 3834.2 doublet was identified in their CSs, but this is sufficient to classify these stars as also belonging to the O(H)-Type. In M 4-2 only a faint blue continuum could be identified as coming from the CS, so this star remains without classification.

6 SELF-CONSISTENT PHOTOIONIZATION MODELLING

Integral field spectroscopy of PNe in our Galaxy presents an ideal opportunity to build fully self-consistent photoionization models. Not only can a global spectrum be extracted which is directly comparable to the theoretical model, but we are able to use the size and morphology to constrain the photoionization structure and inner and outer boundaries of the nebula. In addition, we can directly compare measured electron temperatures and densities in the different ionization zones to constrain the pressure distribution within the ionized material. In this section, we describe how such self-consistent photoionization modelling can provide a good description to all these parameters, while at the same time enabling us to derive chemical abundances, to derive distances, and to place the CSs on the Hertzsprung–Russell (H-R) diagram. We refer the reader to earlier work of this nature on the PN NGC 6828 by Surendiranath & Pottasch (2008).

We have used the MAPPINGS 5.0 code (Sutherland et al., in preparation).[7] Earlier versions of this code have been used to construct photoionization models of H II regions, PNe, Herbig–Haro objects, supernova remnants, and narrow-line regions excited by AGN. This code is the latest version of the MAPPINGS 4.0 code earlier

[6] The identification of this line was determined from the Kentucky data base http://www.pa.uky.edu/~peter/atomic/

[7] Available at miocene.anu.edu.au/Mappings

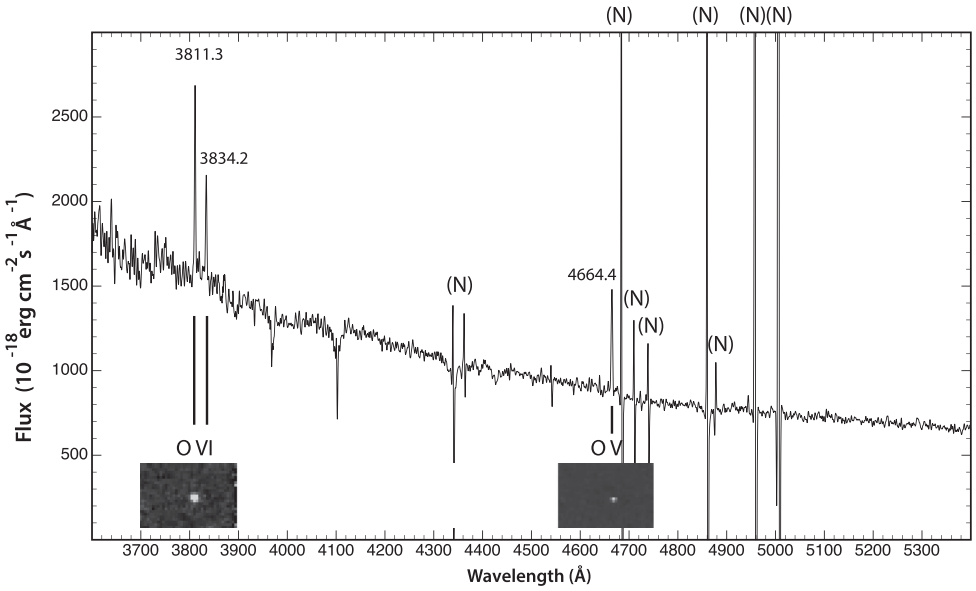

Figure 4. The nebular subtracted spectrum of the CS in NGC 5979 (showing the full WiFeS image field). Emission lines of O VI and O V are clearly detected in the CS, as indicated in the monochromatic thumbnail images shown in the lower part of the figure. The features marked (N) are improperly subtracted nebular features. There are broad Balmer absorption features present in the blue continuum of the star.

described in Dopita et al. (2013), and includes many upgrades to both the input atomic physics and the methods of solution.

We choose for the initial abundance set in the models a value of 0.8 times local galactic concordance abundances based upon the Nieva & Przybilla (2012) data on early B-star data. The Nieva & Przybilla (2012) data provide the abundances of the main coolants, H, He, C, N, O, Ne, Mg, Si, and Fe and the ratios of N/O and C/O as a function of abundance. For the light elements we use the Lodders, Palme & Gail (2009) abundance, while for all other elements the abundances are based upon Scott et al. (2015a,b) and Grevesse et al. (2010). The individual elemental abundances are then iterated from this initial set.

The elemental depletions on to dust grains must be taken into account. Not only do these remove coolants from the nebular gas, but in PNe they are also an important source of photoelectric heating (Dopita & Sutherland 2000). For the depletion factors we use the Jenkins (2009) scheme, with a base depletion of Fe of 1.5 dex. For the dust model, we use a standard Mathis, Rumpl & Nordsieck (1977) dust grain size distribution.

For the spectral energy distribution of the CS, we use the Rauch (2003) model grid, which provide metal-line blanketed Non-Local Thermodynamic Equilibrium (NLTE) model atmospheres for the full range of parameters appropriate to the CSs of PNe. Our initial estimate uses the $\log g = 6.0$ models.

The pressure in the ionized gas is an important parameter. In the modelling, we have used the isobaric approximation (which includes any effect of radiation pressure), and we have matched the pressure to fit the electron densities derived from observation, given in Table 3. In this table, we have also listed the electron densities (and electron temperatures) returned from our 'best-fitting' models. Generally speaking, the agreement is good to a few per cent.

It is clear from the optical morphology given in Fig. 1 that all four of our nebulae are optically thin to the escape of ionizing photons, some more than others. We therefore developed a two-component model consisting of the weighted mean of an optically thin component and an optically thick component.

In addition to the chemical abundance set, the gas pressure, and the fraction of optically thin gas F, the parameters which determine the relative line intensities in the model are the stellar effective temperature $T_{\rm eff}$, the ionization parameter at the inner boundary of the PNe, $U_{\rm in}$ and the fraction of the Strömgren radius ($R_{\rm S}$) at which the outer boundary of the optically thin component is located $f_{\rm S} = R_{\rm out}/R_{\rm S}$. The objective of the modelling is to produce a unique solution to each of these variables.

The strength of the emission lines of low excitation such as [N II], [S II], and [O II] is very sensitive to the fraction of optically thick gas present, and these therefore provide an excellent constraint on F. A further constrain on F is furnished by the [O III]/Hβ ratio, since this first increases, and then sharply decreases as the nebula becomes increasingly optically thin. All four of our PNe are located close to the maximum in the [O III]/Hβ ratio that is observed in PNe. In addition, the helium and hydrogen excitation as measured by the He II λ4686/He I λ5876 and the He I λ5876/Hβ ratios is sensitive to both $T_{\rm eff}$ and $U_{\rm in}$. For a given $f_{\rm S}$, there is a narrow strip of allowed solutions with $\log U_{\rm in}$ falling as $T_{\rm eff}$ rises.

In order to measure the goodness of fit of any particular photoionization model, we measure the L1-norm for the fit. That is to say that we measure the modulus of the mean logarithmic difference in flux (relative to Hβ) between the model and the observations, namely

$$\mathrm{L1} = \Sigma_n \left| \log \left[\frac{F_n(\mathrm{model})}{F_n(\mathrm{obs.})} \right] \right| / n, \qquad (2)$$

where n is the number of lines being considered in the fit. This weights fainter lines equally with stronger lines, and is therefore more sensitive to the values of the input parameters. (By themselves, the stronger lines would not provide sufficient constraints on the variables of the photoionization models, and the signal-to-noise in our spectra is very adequate to measure these fainter lines with sufficient accuracy – see Table A1.) Typically, we simultaneously fit between 27 and 35 emission lines.

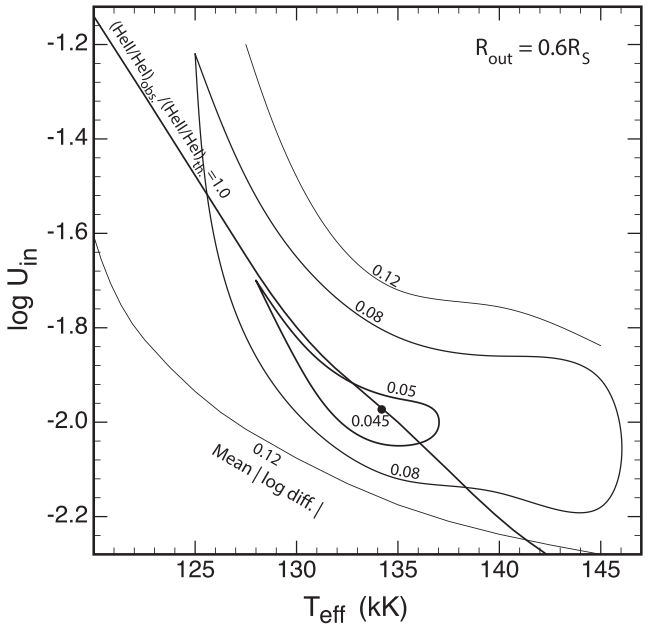

Figure 5. The best-fitting solution for M 4-2 is shown here on the log $U_{\rm in}$ and $T_{\rm eff}$ plane. We seek to minimize the L1-norm (contours), here given by fitting 35 lines, while simultaneously matching the He II, He I, and H II excitation to that observed in the nebula.

For a given $f_{\rm S}$, we ran an extensive grid of models in log $U_{\rm in}$ and $T_{\rm eff}$, and searched for the region where the L1-norm was minimized at the same time as the helium excitation matching the observed value. When this point was identified, we iterated the abundance set in a restricted log $U_{\rm in}$ and $T_{\rm eff}$ range to improve on the L1-norm. Typically, we could reduce this to about 0.05 dex, the error being mostly dominated by a few lines for which apparently the models are inadequate. These are discussed below.

In Fig. 5, we show the solution in the case of M 4-2. For this model, we also provide in Fig. 6 a comparison between the theoretical model (including the CS) and the observations. Here we have matched the resolution of the theoretical spectrum to that of the observations, as best as we can. Note that the flux scale is logarithmic and covers nearly 4 dex. The MAPPINGS 5.0 code does not provide predictions for the higher Balmer and He II $n = 5$ series, as these become sensitive to the density. Nor does the code predict the intensities of the recombination lines of highly ionized species such as the N III, C III, C IV, O V, and O VI lines discussed above. This is simply because the appropriate recombination coefficients and other atomic data are not available for these transitions in these ions. Normally, the recombination coefficients into the excited states would be estimated from the photoionization cross-sections using the Milne relation. However, there are no published estimates of photoionization cross-sections from these excited states. Furthermore, the population of the upper level is also determined by the cascade from more highly excited states, as well as by collisional contributions from the lower levels. Finally, for some excited levels radiative transfer effects (e.g. case A or B) can make large differences to the predicted recombination line strengths, and UV pumping into upper states followed by radiative cascade into the upper state of the transition being considered can also be very important. Apart from these issues, which regrettably specifically affect the characteristic WELS recombination lines, the overall fit of the model to the observation is excellent.

The derived parameters for the 'best-fitting' final models are given in Table 7.

In Table 8, we present a comparison of the observed and modelled line intensities of the lines used in the fitting. Overall, the agreement between the model and the observations is good. However, we note a systematic effect that limits the minimum value of the L1-norm. Although the predicted [Ne III] line intensities are satisfactory, the [Ne V] lines are too weak with respect to the [Ne IV] lines, while at the same time the [Ar V] lines are too strong with respect to the [Ar IV] lines. The ionization potential of Ne III is 63.45 eV, that of Ne IV is 97.12 eV, and that of Ar IV is 59.81 eV. These are all high, but in the same general range. Thus, the differences between the predictions and the observations cannot probably be ascribed to differences in the input ionizing spectra, but are more likely caused by errors in the charge exchange reaction rates used by the code, which will affect the detailed ionization balance in the nebula.

6.1 Distances from photoionization models

In this section, we will develop on a method to estimate distances based only upon the requirement that the model reproduce both the observed flux and the observed angular size of the PN. The success of this method depends critically on how well we have determined $f_{\rm S}$, since this will in turn determine the relationship between the luminosity of the CS and the absolute Hβ luminosity of the nebula. Our model, in essence, consists of the application of simple Strömgren theory. For a given electron density $n_{\rm e}$ and nebular radius, r, the Hβ luminosity $L_{\rm H\beta}$ is given by

$$L_{\rm H\beta} \propto n_{\rm e}^2 r^3 \tag{3}$$

and the angular radius θ is given in terms of the distance d, $\theta = r/d$. The reddening-corrected observed Hβ luminosity $F_{\rm H\beta}$ is given by

$$F_{\rm H\beta} = L_{\rm H\beta}/(4\pi d^2). \tag{4}$$

Our photoionization models give (for any assumed distance and stellar luminosity L_*) the values of $L_{\rm H\beta}$, r and $n_{\rm e}$, and the observations give us $F_{\rm H\beta}$ and θ, so from these equations we can solve for the distance at which the model predicted angular radius θ and Hβ flux agree with the observed values. Note that the solution depends critically on the accurate determination of the parameter $f_{\rm S}$, which affects both the absolute flux and the radius of the model, and on log P/k, which also has a strong effect on the radius predicted by the model for any assumed stellar luminosity. Observationally, the error in the determination of $F_{\rm H\beta}$ is not of concern, but the error in the determination of θ has a much greater effect on the solution, since the nebular boundary is not always clearly defined. Where possible, we have used the angular radius for the optically thick part of the nebula, as measured in the [N II] line, but for NGC 5979 and My 60 we have used the angular diameter as measured in the Hα line.

The solutions for the distance of each PN are given graphically in Fig. 7. The distances derived by this method are as follows, where the mean of the statistical distance scale estimates is given in parentheses. NGC 3211: $3.6^{+1.05}_{-0.96}$ kpc (2.61 kpc); NGC 5979: $2.4^{+0.9}_{-0.6}$ kpc (2.99 kpc); My 60: $4.0^{+1.1}_{-0.8}$ kpc (3.76 kpc); M 4-2: $5.5^{+1.7}_{-1.5}$ kpc (5.90 kpc). In each case, the agreement with the statistical distance estimate is within the error bar. This gives confidence in the validity of the method. None the less, due to both the modelling errors and the observational limitations mentioned above, we conclude that this method cannot deliver sufficient accuracy to supplant the

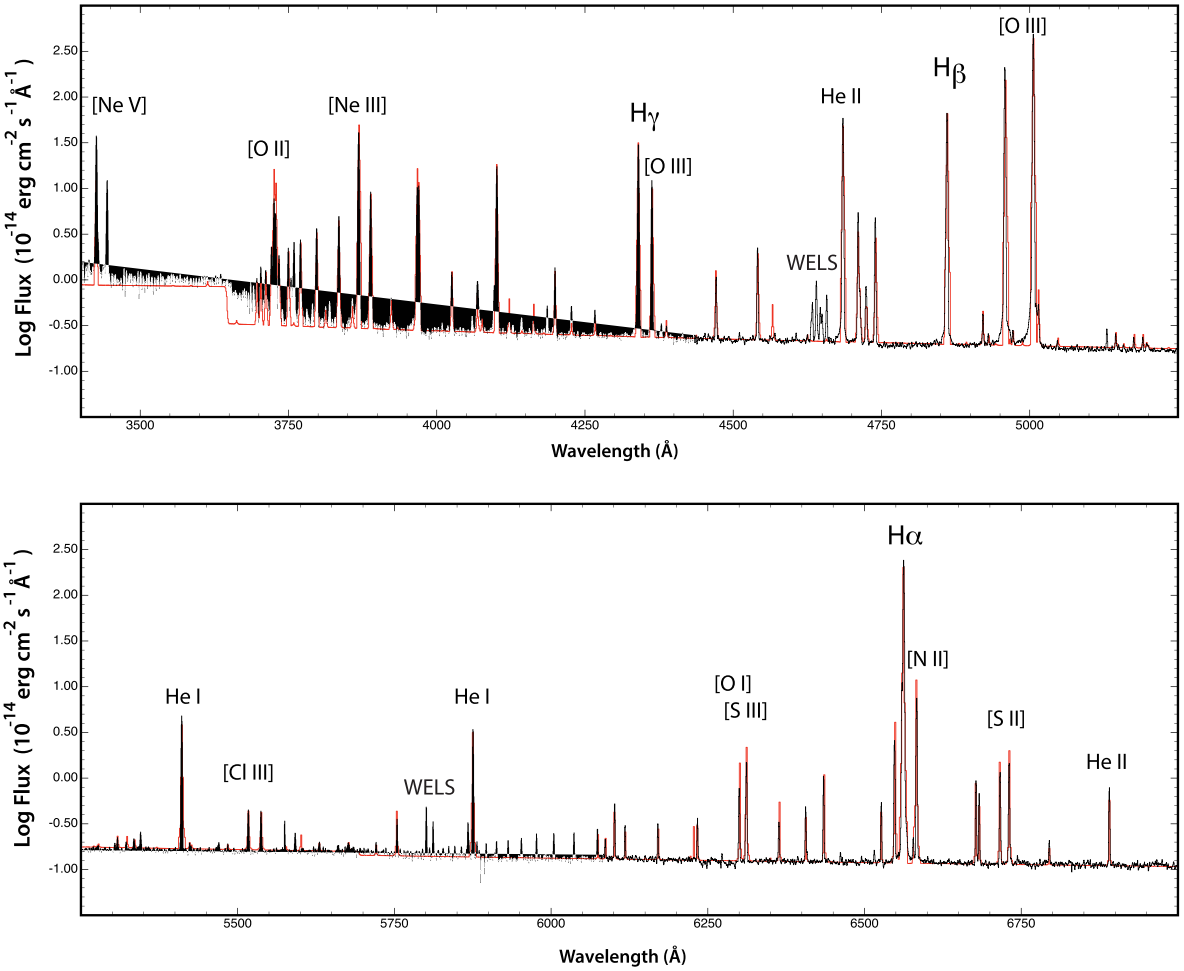

Figure 6. The comparison between the observed (de-reddened) global spectrum of M 4-2 (PN G248.8−08.5) (black) and the best-fitting MAPPINGS 5.0 photoionization model (red). Some of the principal emission lines are identified. Note the excellent agreement between the observed and the theoretical nebular + stellar continuum, which is only possible when the observed spectrum has been correctly de-reddened.

Table 7. Derived parameters for the best-fitting final models.

	log P/k (cm^{-3} K)	F	f_S	log U_{in}	T_{eff} (kK)
NGC 3211	7.63	0.992	0.72	−1.95	145
NGC 5979	7.62	1.00	0.64	−1.60	160
My 60	7.72	1.00	0.60	−1.55	130
M 4-2	7.73	0.935	0.60	−1.90	134

statistical distance estimate techniques, but is certainly sufficient to provide an independent check on these.

At these distances, the nebular diameters (D) as given from the photoionization model are as follows: $D = 0.138$ pc for NGC 3211, 0.174 pc for NGC 5979, 0.153 pc for My 60, and 0.237 pc for M 4-2. In the case of NGC 3211, the diameter is measured to the edge of the [N II] zone, while in the other three objects the diameter refers to the diameter of the optically thin region.

6.2 Location of CSs on the H-R diagram

With reasonably accurate knowledge of the distance, we can now place the CSs on the H-R diagram. For this purpose, we adopt a mean of the statistical and photoionisation distances: $3.2^{+1.2}_{-1.0}$ kpc for NGC 3211, $2.7^{+1.0}_{-0.7}$ kpc for NGC 5979, $3.9^{+1.1}_{-0.8}$ kpc for My 60, and $5.8^{+1.7}_{-1.5}$ kpc for M 4-2. With these distances, we derive stellar luminosities and their errors, and from the models, we also provide the derived stellar temperatures with their estimated measurement errors. These are given in Table 9.

In Fig. 8, we locate these stars on the H-R diagram. Overlaid are the H-burning $Z = 0.016$ tracks from Vassiliadis & Wood (1994). What is remarkable is the manner in which the four objects of our study cluster tightly together, suggesting very similar precursor stars. All are consistent with having initial masses between 1.5 and 2.0 $M_\odot$, and having an evolutionary age of about 6000 yr. It is interesting that the only bona fide double-shell PN, NGC 5979, seems to have the highest mass precursor. This would be consistent with the evolutionary scenario of Vassiliadis & Wood (1993), in that the He-shell flashes occur more frequently in higher mass precursors, driving 'super-wind' episodes which then form multiple shells in the subsequent PNe.

The age of the PNe as measured from the H-burning tracks is in fact the time since the CS became hotter than 10^4 K. This can be directly compared to the estimated dynamical ages given from the diameters given above, and the expansion velocity in the low-ionization species as given in Table 6. These are, respectively,

Table 8. Line fluxes, relative to Hβ = 100, from photoionization models compared with those observed in NGC 3211, NGC 5979, My 60, and M 4-2.

		NGC 3211		NGC 5979		My 60		M 4-2	
Lab (Å)	ID	Model	Observed	Model	Observed	Model	Observed	Model	Observed
3425.88	[Ne V]	45.23	71.4 ± 2.95	54.31	58.6 ± 3.49	21.44	26.2 ± 1.60	19.5	61.4 ± 2.44
3726.03	[O II]	33.32	17.4 ± 0.66	18.2	3.4 ± 0.19	15.10	5.2 ± 0.36	15.34	11.8 ± 0.43
3728.82	[O II]	24.3	12.4 ± 0.47	12.2	2.3 ± 0.13	10.00	3.0 ± 0.20	9.75	7.5 ± 0.32
3770.63	H I 11-2	3.89	4.4 ± 0.26	3.96	3.6 ± 0.19	3.98	3.6 ± 0.25	3.84	3.9 ± 0.17
3835.39	H I 9-2	7.19	8.5 ± 0.31	7.30	7.3 ± 0.39	7.34	7.8 ± 0.43	7.09	7.7 ± 0.32
3868.76	[Ne III]	173.7	112.4 ± 4.1	62.44	58.4 ± 3.12	109.6	90.3 ± 4.96	86.30	65.3 ± 2.34
3889.06	H I 8-2	10.34	16.4 ± 0.60	10.49	11.5 ± 0.62	10.55	15.8 ± 0.85	10.2	14.5 ± 0.52
3967.47	[Ne III]	52.35	36.5 ± 1.30	16.8	17.5 ± 0.91	33.02	22.9 ± 1.24	26.01	15.9 ± 0.56
3970.08	H I 7-2	15.68	15.8 ± 0.56	15.89	14.3 ± 0.75	15.99	15.3 ± 0.80	15.46	15.5 ± 0.54
4068.60	[S II]	1.01	1.8 ± 0.10	0.20	1.3 ± 0.07	0.20	2.0 ± 0.16	0.34	2.4 ± 0.10
4076.35	[S II]	0.32	0.4 ± 0.04	0.07	0.1 ± 0.02	0.06	–	0.11	–
4267.14	C II	0.15	0.5 ± 0.05	0.80	0.8 ± 0.05	0.55	0.6 ± 0.12	0.90	0.9 ± 0.08
4340.47	H I 5-2	46.98	49.2 ± 1.52	47.11	44.4 ± 2.05	47.16	48.3 ± 2.30	47.05	47.2 ± 1.47
4363.21	[O III]	22.75	25.1 ± 0.81	14.78	14.7 ± 0.70	18.01	18.9 ± 0.92	14.91	17.6 ± 0.56
4471.50	He I	1.98	1.8 ± 0.10	0.70	0.8 ± 0.05	2.11	2.2 ± 0.17	1.32	1.3 ± 0.12
4541.59	He II	2.65	2.9 ± 0.16	3.59	3.7 ± 0.17	2.68	2.9 ± 0.18	0.88	2.9 ± 0.11
4685.70	He II	86.21	85.3 ± 2.52	105.1	105.5 ± 4.67	78.48	80.4 ± 3.59	84.93	83.8 ± 2.47
4711.26	[Ar IV]	8.20	11.0 ± 0.33	8.56	14.2 ± 0.63	7.17	10.7 ± 0.47	5.46	7.5 ± 0.28
4714.50	[Ne IV]	0.68	1.5 ± 0.08	0.32	1.2 ± 0.05	0.34	–	1.86	1.0 ± 0.09
4724.89	[Ne IV]	1.24	2.0 ± 0.11	0.52	1.9 ± 0.08	0.57	1.3 ± 0.10	1.20	1.4 ± 0.13
4740.12	[Ar IV]	6.90	9.6 ± 0.28	7.45	12.1 ± 0.53	6.46	9.4 ± 0.41	6.90	6.5 ± 0.24
4861.33	H I 4-2	100.0	100.0 ± 0.0	100.0	100.0 ± 0.0	100.0	100.0 ± 0.0	100.0	100.0 ± 0.0
4958.91	[O III]	399.1	528.5 ± 14.6	312.0	304.0 ± 12.7	396.0	422.6 ± 17.7	237.7	304.0 ± 8.4
5006.84	[O III]	1153.9	1512 ± 42	901.8	905.8 ± 37	1145.0	1184.9 ± 47	687.0	870.8 ± 24
5411.52	He II	6.07	6.3 ± 0.17	8.26	8.6 ± 0.33	6.17	6.3 ± 0.24	2.02	6.3 ± 0.21
5517.71	[Cl III]	1.0	1.0 ± 0.10	0.50	0.5 ± 0.03	0.49	0.5 ± 0.05	0.43	0.4 ± 0.04
5537.87	[Cl III]	0.90	0.9 ± 0.09	0.48	0.5 ± 0.03	0.51	0.5 ± 0.05	0.42	0.4 ± 0.04
5875.66	He I	5.74	4.8 ± 0.13	2.02	2.0 ± 0.06	6.14	6.2 ± 0.18	3.86	3.9 ± 0.10
6086.97	[Fe VII]	0.11	0.1 ± 0.02	0.09	0.1 ± 0.00	0.10	0.1 ± 0.01	0.10	0.1 ± 0.02
6101.83	[K IV]	0.53	0.5 ± 0.05	0.70	0.7 ± 0.03	0.6	0.5 ± 0.02	0.50	0.5 ± 0.02
6300.30	[O I]	0.20	0.2 ± 0.02	0.04	–	0.02	–	0.73	0.8 ± 0.02
6312.06	[S III]	8.30	3.2 ± 0.09	1.82	1.8 ± 0.05	2.21	1.6 ± 0.05	2.75	1.8 ± 0.03
6363.78	[O I]	0.08	0.1 ± 0.02	0.01	–	0.01	–	0.24	0.3 ± 0.03
6433.12	[Ar V]	2.11	1.0 ± 0.10	3.79	1.7 ± 0.05	2.07	0.8 ± 0.03	0.31	1.0 ± 0.03
6548.05	[N II]	4.22	5.8 ± 0.17	0.78	0.7 ± 0.03	1.22	1.1 ± 0.03	3.72	4.2 ± 0.07
6560.09	He II	10.38	9.7 ± 0.28	14.2	12.7 ± 0.39	10.61	9.5 ± 0.27	10.2	11.5 ± 0.19
6562.82	H I 3-2	288.3	286.7 ± 3.4	284.0	274.7 ± 4.3	282.1	283.1 ± 3.1	286.7	278.8 ± 2.6
6583.45	[N II]	12.43	15.5 ± 0.45	2.31	2.4 ± 0.07	3.58	3.5 ± 0.10	10.92	10.4 ± 0.17
6678.15	He I	0.93	1.3 ± 0.13	0.49	0.5 ± 0.03	1.47	1.6 ± 0.05	0.90	1.0 ± 0.02
6683.45	He II	0.53	0.5 ± 0.05	0.72	0.8 ± 0.04	0.54	0.6 ± 0.02	0.5	0.6 ± 0.03
6716.44	[S II]	3.90	2.7 ± 0.15	0.68	0.6 ± 0.03	0.59	0.6 ± 0.02	0.89	1.3 ± 0.02
6730.82	[S II]	4.86	3.2 ± 0.10	0.93	0.7 ± 0.03	0.86	0.8 ± 0.03	1.19	1.7 ± 0.03
6795.16	[K IV]	0.1	0.1 ± 0.01	0.21	0.2 ± 0.01	0.1	0.1 ± 0.01	0.03	0.1 ± 0.02
6890.91	He II	0.68	0.7 ± 0.07	0.92	1.0 ± 0.05	0.69	0.7 ± 0.02	0.22	0.8 ± 0.03
7005.83	[Ar V]	4.61	1.8 ± 0.10	8.05	3.5 ± 0.11	4.41	1.8 ± 0.05	11.97	2.1 ± 0.05

$\tau_{\rm dyn}$ = 3000 yr for NGC 3211, 3950 yr for NGC 5979, 3100 yr for My 60, and 4500 yr for M 4-2. The dynamical ages are somewhat shorter than the age implied from the evolutionary tracks, but both methods agree that the ages of these four PNe are very similar. Due to acceleration or deceleration of the nebular shell, driven by the changing stellar wind parameters during its dynamical evolution, we have no reason to expect that the dynamical age derived will be exactly equal to the age inferred by the position of the PN on the evolutionary track. Thus, we see no serious discrepancy between the dynamical and the evolutionary age. If we were to use the recent models of Miller Bertolami (2016), then the observed dynamical ages would show closer agreement to the theoretical ages derived from the position of PNe along the post-AGB track.

7 CONCLUSIONS

In this paper, we have studied four PNe, three of which had been classified with CSs of the WELS type, and the fourth which showed the same set of recombination lines of highly excited ions which are thought to characterize a WELS: C IV at 5801–12 Å and the N III, C III, and C IV complex feature at 4650 Å. We have, however, demonstrated that these emission lines arise not in the CS, but are instead distributed throughout the nebular gas. We find no trace of these emission originating from the CSs themselves. Instead, we identify O VI λλ3811.3, 3834.2 in three of the CSs, and in the case of NGC 5979 the O V λ4664.4 line as well. Thus, at least three of the CSs are not WELS, but are in fact hot O(H) stars. This result casts doubt on the reality of the WELS class as a whole, a result made

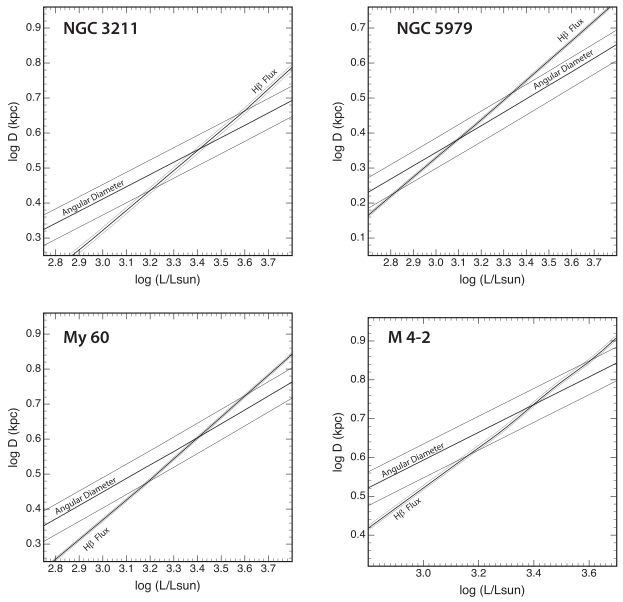

Figure 7. The solution to the absolute luminosity and distance of the PNe given by the requirement that both the reddening-corrected observed Hβ flux and the observed angular size of the PNe agree with those predicted by the photoionization model. The error bands are the measurement errors of the observed quantities.

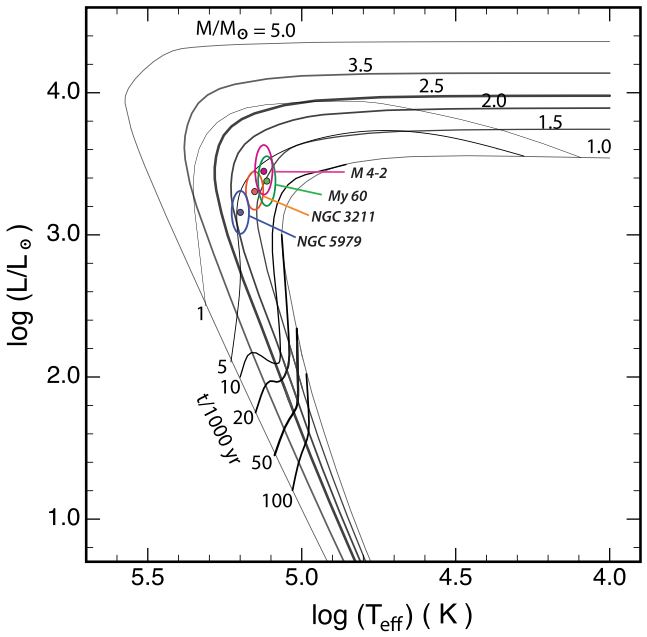

Figure 8. The location of our PNe on the (hydrogen-burning) H-R diagram as derived from photoionization modelling compared with evolutionary tracks of CSs of PNe from Vassiliadis & Wood (1994). The four objects are remarkably similar, and consistent with having initial masses in the range 1.5–2.0 $M_{\odot}$, and evolutionary ages of about 6000 yr.

Table 9. Derived CS parameters.

	log L ($L_{\odot}$)	log $T_{\rm eff}$ (K)
NGC 3211	$3.30^{+0.13}_{-0.13}$	$5.16^{+0.03}_{-0.03}$
NGC 5979	$3.18^{+0.15}_{-0.15}$	$5.20^{+0.03}_{-0.03}$
My 60	$3.39^{+0.17}_{-0.17}$	$5.11^{+0.03}_{-0.03}$
M 4-2	$3.44^{+0.20}_{-0.18}$	$5.13^{+0.03}_{-0.03}$

possible only by the fact that we have integral field spectroscopy covering the whole nebula.

We cannot use nebular emission-line characteristics to define a class of the CS, since the nebular lines depend on the nature of the EUV spectrum, the chemical abundances, the density and the geometry of the gas with respect to the CS. We always define the CS type itself from the UV, visible, or IR emissions of the CS. If the emission lines which have been used to classify the star instead arise in the nebula, as we have demonstrated here in four independent examples, then the classification has no validity. Clearly, as in the case of binary systems, some real examples of WELS exist. However, given that we have found four out of four examples of misclassification, we believe that many other cases of such misclassification may exist. This is the major conclusion of this paper.

As to why the C IV at 5801–12 Å and the N III, C III, and C IV complex feature at 4650 Å are so strong, we cannot provide a solution, since we do not have the required atomic data relating to the effective recombination coefficients. It may be possible that we have C- and N-rich pockets of gas in the nebula, but then why would these species be distributed in exactly the way we would expect in terms of the local excitation? Figs 1 and 3 are remarkably similar.

Apart from the standard nebular analysis techniques used to probe chemical abundances and physical conditions in the nebula, we have been able to apply self-consistent photoionization modelling to an analysis of the integrated spectrum of these PNe. We find that an optically thin isobaric model with an inner empty zone and, in some cases, an additional optically thick zone provides an excellent description of the observed spectrum, and provides a good estimate of the stellar effective temperature. Generally speaking, the agreement between the two analysis methods is quite satisfactory as far as the abundance determinations are concerned.

According to the derived chemical abundances from the NEAT, none of our objects was classified as Type I PN. We find that the chemical compositions of both NGC 3211 and NGC 5979 are consistent with being of Type IIa, while that of My 60 and M 4-2 are consistent with the Type IIb/III classification. Considering also their calculated Galactic vertical heights and peculiar velocities, we suggest that NGC 3211 is probably a member of the Galactic thin disc, while both My 60 and M 4-2 are Galactic thick members.

Additionally, the self-consistent modelling yields a number of additional parameters. Specifically, we are able to use the models to provide a new 'Strömgren distance' estimate, which agrees – within the errors – with the distances derived from the standard statistical techniques. We find that all four PNe are highly excited nebulae optically thin to the escape of EUV photons. With knowledge of the distance, another parameter derived from the models, we are also able to constrain the luminosity of the CS, placing it on the H-R diagram.

All four PNe studied in this paper are of remarkably similar $T_{\rm eff}$ and luminosity, are at a very similar evolutionary stage with ages in the range 3000–6000 yr, and are all derived from precursor stars in the restricted mass range 1.5–2.0 $M_{\odot}$.

ACKNOWLEDGEMENTS

The authors would like to thank the anonymous referee for valuable and constructive comments.

REFERENCES

Acker A., Neiner C., 2003, A&A, 403, 659
Acker A., Raytchev B., Stenholm B., Tylenda R., 1991, A&AS, 90, 89
Ali A., Ismail H. A., Alsolami Z., 2015a, Ap&SS, 357, 21
Ali A., Amer M. A., Dopita M. A., Vogt F. P. A., Basurah H. M., 2015b, A&A, 583, A83
Aller L. H., 1956, Gaseous Nebulae. Chapman & Hall, London
Baessgen M., Grewing M., 1989, A&A, 218, 273
Balick B., Rugers M., Terzian Y., Chengalur J. N., 1993, ApJ, 411, 778
Balick B., Perinotto M., Maccioni A., Terzian Y., Hajian A., 1994, ApJ, 424, 800
Balick B., Alexander J., Hajian A. R., Terzian Y., Perinotto M., Patriarchi P., 1998, AJ, 116, 360
Campbell W. W., Moore J. H., 1918, Publ. Lick Obs., 13, 75
Childress M. J., Vogt F. P. A., Nielsen J., Sharp R. G., 2014, Ap&SS, 349, 617
Corradi R. L. M., Schönberner D., Steffen M., Perinotto M., 2003, MNRAS, 340, 417
Corradi R. L. M., Steffen M., Schönberner D., Jacob R., 2007, A&A, 474, 529
Corradi R. L. M. et al., 2011, MNRAS, 410, 1349
Crowther P. A., De Marco O., Barlow M. J., 1998, MNRAS, 296, 367
Danehkar A., Parker Q. A., 2015, MNRAS, 449, L56
Danehkar A., Parker Q. A., Ercolano B., 2013, MNRAS, 434, 1513
Danehkar A., Todt H., Ercolano B., Kniazev A. Y., 2014, MNRAS, 439, 3605
Dopita M. A., 1997, ApJ, 485, L41
Dopita M. A., Sutherland R. S., 2000, ApJ, 539, 742
Dopita M., Hart J., McGregor P., Oates P., Bloxham G., Jones D., 2007, Ap&SS, 310, 255
Dopita M. et al., 2010, Ap&SS, 327, 245
Dopita M. A., Sutherland R. S., Nicholls D. C., Kewley L. J., Vogt F. P. A., 2013, ApJS, 208, 10
Durand S., Acker A., Zijlstra A., 1998, A&AS, 132, 13
Fogel J., De Marco O., Jacoby G., 2003, in Kwok S., Dopita M., Sutherland R., eds, Proc. IAU Symp. 209, Planetary Nebulae: Their Evolution and Role in the Universe. Astron. Soc. Pac., San Francisco, p. 235
Frew D. J., Parker Q. A., 2010, PASA, 27, 129
Frew D. J., Parker Q. A., 2012, in Manchado A., Stanghellini L., Schönberner D., eds, Proc. IAU Symp. 283, Planetary Nebulae: An Eye to the Future. Cambridge Univ. Press, Cambridge, p. 192
Frew D. J., Parker Q. A., Bojičić I. S., 2016, MNRAS, 455, 1459
Gathier R., Pottasch S. R., 1989, A&A, 209, 369
Gathier R., Pottasch S. R., Pel J. W., 1986, A&A, 157, 171
Gieseking F., Hippelein H., Weinberger R., 1986, A&A, 156, 101
Girard P., Köppen J., Acker A., 2007, A&A, 463, 265
Górny S. K., 2014, A&A, 570, A26
Górny S. K., Schwarz H. E., Corradi R. L. M., Van Winckel H., 1999, A&AS, 136, 145
Grevesse N., Asplund M., Sauval A. J., Scott P., 2010, Ap&SS, 328, 179
Gruenwald R., Viegas S. M., 1995, A&A, 303, 535
Gurzadian G. A., 1988, Ap&SS, 149, 343
Hajduk M., Zijlstra A. A., Gesicki K., 2010, MNRAS, 406, 626
Hajian A. R., Balick B., Terzian Y., Perinotto M., 1997, ApJ, 487, 304
Hajian A. R. et al., 2007, ApJS, 169, 289
Henry R. B. C., Kwitter K. B., Balick B., 2004, AJ, 127, 2284
Howarth I. D., 1983, MNRAS, 203, 301
Jenkins E. B., 2009, ApJ, 700, 1299
Kaler J. B., Kwitter K. B., Shaw R. A., Browning L., 1996, PASP, 108, 980
Kingsburgh R. L., Barlow M. J., 1994, MNRAS, 271, 257
Liu X.-W., Danziger J., 1993, MNRAS, 263, 256
Lodders K., Palme H., Gail H.-P., 2009, Landolt Börnstein, 44
Maciel W. J., Quireza C., 1999, A&A, 345, 629
Marcolino W. L. F., de Araújo F. X., 2003, AJ, 126, 887
Marcolino W. L. F., de Araújo F. X., Junior H. B. M., Duarte E. S., 2007, AJ, 134, 1380
Mathewson D. S., Hart J., Wehner H. P., Hovey G. R., van Harmelen J., 2013, J. Astron. Hist. Herit., 16, 2
Mathis J. S., Rumpl W., Nordsieck K. H., 1977, ApJ, 217, 425
Meatheringham S. J., Dopita M. A., 1991, ApJS, 75, 407
Meatheringham S. J., Wood P. R., Faulkner D. J., 1988, ApJ, 334, 862
Mendez R. H., 1991, in Michaud G., Tutukov A. V., eds, Proc. IAU Symp. 145, Evolution of Stars: The Photospheric Abundance Connection. Kluwer, Dordrecht, p. 375
Milingo J. B., Henry R. B. C., Kwitter K. B., 2002, ApJS, 138, 285
Miller Bertolami M. M., Viallet M., Prat V., Barsukow W., Weiss A., 2016, MNRAS, 457, 4441
Miszalski B., 2009, PhD thesis, Department of Physics, Macquarie University
Miszalski B., Corradi R. L. M., Boffin H. M. J., Jones D., Sabin L., Santander-García M., Rodríguez-Gil P., Rubio-Díez M. M., 2011, MNRAS, 413, 1264
Monreal-Ibero A., Roth M. M., Schönberner D., Steffen M., Böhm P., 2005, ApJ, 628, L139
Monteiro H., Gonçalves D. R., Leal-Ferreira M. L., Corradi R. L. M., 2013, A&A, 560, A102
Nieva M.-F., Przybilla N., 2012, A&A, 539, A143
Parthasarathy M., Acker A., Stenholm B., 1998, A&A, 329, L9
Peimbert M., 1978, in Terzian Y., ed., Proc. IAU Symp. 76, Planetary Nebulae. Reidel, Dordrecht, p. 215
Peimbert M., Torres-Peimbert S., 1983, in Flower D. R., ed., Proc. IAU Symp. 103, Planetary Nebulae. Reidel, Dordrecht, p. 233
Peimbert M., Torres-Peimbert S., 1987, Rev. Mex. Astron. Astrofis., 14, 540
Perinotto M., 1991, ApJS, 76, 687
Phillips J. P., 2000, AJ, 119, 2332
Quireza C., Rocha-Pinto H. J., Maciel W. J., 2007, A&A, 475, 217
Rauch T., 2003, A&A, 403, 709
Reid W. A., Parker Q. A., 2010, PASA, 27, 187
Ruffle P. M. E., Zijlstra A. A., Walsh J. R., Gray M. D., Gesicki K., Minniti D., Comeron F., 2004, MNRAS, 353, 796
Schneider S. E., Terzian Y., 1983, ApJ, 274, L61
Schönberner D., Jacob R., Steffen M., 2005, A&A, 441, 573
Schwarz H. E., Corradi R. L. M., Melnick J., 1992, A&AS, 96, 23
Scott P. et al., 2015a, A&A, 573, A25
Scott P., Asplund M., Grevesse N., Bergemann M., Sauval A. J., 2015b, A&A, 573, A26
Shaw R. A., Kaler J. B., 1989, ApJS, 69, 495
Stanghellini L., Corradi R. L. M., Schwarz H. E., 1993, A&A, 279, 521
Stanghellini L., Shaw R. A., Mutchler M., Palen S., Balick B., Blades J. C., 2002, ApJ, 575, 178
Surendiranath R., Pottasch S. R., 2008, A&A, 483, 519
Tsamis Y. G., Walsh J. R., Pequignot D., Barlow M. J., Liu X.-W., Danziger I. J., 2007, The Messenger, 127, 53
Tylenda R., Acker A., Stenholm B., Koeppen J., 1992, A&AS, 95, 337
Tylenda R., Acker A., Stenholm B., 1993, A&AS, 102, 595
Vassiliadis E., Wood P. R., 1993, ApJ, 413, 641
Vassiliadis E., Wood P. R., 1994, ApJS, 92, 125
Wang W., Liu X.-W., Zhang Y., Barlow M. J., 2004, A&A, 427, 873
Weidmann W. A., Gamen R., 2011, A&A, 526, A6
Weidmann W. A., Méndez R. H., Gamen R., 2015, A&A, 579, A86
Werner K., Dreizler S., Heber U., Rauch T., 1997, in Isern J., Hernanz M., Gracia-Berro E., eds, Astrophysics and Space Science Library, Vol. 214, Proc. 10th European Workshop on White Dwarfs. Kluwer Academic Publishers, Dordrecht, p. 207
Wesson R., Stock D. J., Scicluna P., 2012, MNRAS, 422, 3516
Zhang C. Y., 1993, ApJ, 410, 239
Zhang C. Y., Kwok S., 1993, ApJS, 88, 137

Table A1. Line fluxes and de-reddened intensities, relative to Hβ = 100, of NGC 3211, NGC 5979, My 60, and M 4-2. The full version of the table is available online. A portion is shown here for guiding the reader regarding its content.

		NGC 3211		NGC 5979		My 60		M 4-2	
Lab (Å)	ID	$F(\lambda)$	$I(\lambda)$	$F(\lambda)$	$I(\lambda)$	$F(\lambda)$	$I(\lambda)$	$F(\lambda)$	$I(\lambda)$
3868.76	[Ne III]	92.5 ± 1.85	112.4 ± 4.1	47.1 ± 1.41	58.4 ± 3.12	57.2 ± 1.72	90.3 ± 4.96	48.1 ± 0.96	65.3 ± 2.34
3889.06	H I 8-2	13.6 ± 0.27	16.4 ± 0.60	9.3 ± 0.28	11.5 ± 0.62	10.1 ± 0.30	15.8 ± 0.85	10.7 ± 0.21	14.5 ± 0.52
3923.48	He II	0.4 ± 0.04	0.5 ± 0.05	0.6 ± 0.02	0.8 ± 0.04			0.5 ± 0.01	0.7 ± 0.03
3967.47	[Ne III]	30.6 ± 0.61	36.5 ± 1.30	14.4 ± 0.43	17.5 ± 0.91	15.1 ± 0.45	22.9 ± 1.24	12.0 ± 0.24	15.9 ± 0.56
3970.08	H I 7-2	13.2 ± 0.26	15.8 ± 0.56	11.8 ± 0.35	14.3 ± 0.75	10.1 ± 0.30	15.3 ± 0.80	11.8 ± 0.24	15.5 ± 0.54
4025.61	He II							1.5 ± 0.05	2.0 ± 0.08
4026.08	N II	1.5 ± 0.15	1.8 ± 0.19	1.3 ± 0.04	1.5 ± 0.08	1.3 ± 0.13	1.9 ± 0.21		
4068.60	[S II]	1.5 ± 0.08	1.8 ± 0.10	1.1 ± 0.03	1.3 ± 0.07	1.4 ± 0.10	2.0 ± 0.16	1.9 ± 0.06	2.4 ± 0.10

SUPPORTING INFORMATION

Additional Supporting Information may be found in the online version of this article:

Table A1. Line fluxes and de-reddened intensities, relative to Hβ = 100, of NGC 3211, NGC 5979, My 60, and M 4-2. (http://www.mnras.oxfordjournals.org/lookup/suppl/doi:10.1093/mnras/stw468/-/DC1).

Please note: Oxford University Press is not responsible for the content or functionality of any supporting materials supplied by the authors. Any queries (other than missing material) should be directed to the corresponding author for the paper.

APPENDIX A: MEASURED EMISSION-LINE FLUXES

We determined the final integrated emission-line fluxes from the combined, flux-calibrated blue and red spectra of each PN. The line fluxes and their measurement uncertainties were determined using the IRAF `splot`[8] task and were integrated between two given limits, over a local continuum fitted by eye, using multiple Gaussian fitting for the line profile.

The amount of interstellar reddening was determined by the NEAT code from the ratios of hydrogen Balmer lines, in an iterative method. First, the reddening coefficient, $c(\mathrm{H}\beta)$, was calculated assuming intrinsic Hα, Hβ, Hγ line ratios for a temperature (T_e) of 10 000 K and density (N_e) of 1000 cm^{-3}, which were used to de-redden the line list. Secondly, the electron temperature and density were calculated as explained in Section 3.2. After that, the intrinsic Balmer line ratios were re-calculated at the convenient temperature and density, and again $c(\mathrm{H}\beta)$ was re-calculated. The line intensities have been corrected for extinction by adopting the extinction law of Howarth (1983). The estimated reddening coefficients and observed Hβ fluxes of the sample are listed in Table 2, while Table A1 lists the observed and de-reddened line strengths of the sample. Columns (1) and (2) give the laboratory wavelengths and identification of observed emission lines, while columns (3)–(10) give the observed $F(\lambda)$ and the de-reddened line strengths $I(\lambda)$, scaled to Hβ = 100. A total of ∼128 distinct emission lines were identified in each nebula, which include ∼88 permitted and 40 forbidden lines.

[8] IRAF is distributed by the National Optical Astronomy Observatory, which is operated by the Association of Universities for Research in Astronomy (AURA) under a cooperative agreement with the National Science Foundation.

This paper has been typeset from a TEX/LATEX file prepared by the author.